Structural insights into allosteric mechanism of glycine transporter-mediated analgesia

Ryan P. Cantwell Chater[1,2], Julian Peiser-Oliver[2], Tanmay K. Pati[3], Ada S. Quinn[4,5], Irina Lotsaris[2], Zachary J. Frangos[6,7], Anna E. Tischer[6], Billy J Williams-Noonan[4,5], Megan L. O'Mara[4,5], Michael Michaelides[6], Sarasa A. Mohammadi[2], Christopher L. Cioffi[3,*], Robert J. Vandenberg[2,*] & Azadeh Shahsavar[1,*]

[1]Department of Drug Design and Pharmacology, Faculty of Health and Medical Sciences, University of Copenhagen, Copenhagen, Denmark
[2]School of Medical Sciences, University of Sydney, Sydney, NSW, Australia
[3]Department of Chemistry and Chemical Biology, Rensselaer Polytechnic Institute, Troy, New York, USA
[4]Australian Institute of Bioengineering and Nanotechnology, The University of Queensland, St Lucia, Queensland, Australia
[5]ARC Industry Transformation Training Centre for Cryo-electron Microscopy of Membrane Proteins (CCeMMP)
[6]Biobehavioral Imaging & Molecular Neuropsychopharmacology Unit, Neuroimaging Research Branch, National Institute on Drug Abuse, Intramural Research Program, Baltimore, MD, USA
[7]Medication Development Program, National Institute on Drug Abuse, Intramural Research Program

*Correspondence: cioffc4@rpi.edu (CLC), robert.vandenberg@sydney.edu.au (RJV), ash@sund.ku.dk (AS)

Requests for further information and resources should be directed to and will be fulfilled by the lead contact, Azadeh Shahsavar (ash@sund.ku.dk).

SUMMARY

Chronic neuropathic pain, caused by nerve damage or disease, affects 10% of the population with rising incidence. The burden is exacerbated by ineffective treatments and overreliance on opioids. Neuronal glycine transporter, GlyT2, represents a promising target to restore disrupted inhibitory glycinergic neurotransmission in neuropathic pain. However, most GlyT2 inhibitors have not progressed to clinical use because of significant side effects, partly from irreversible inhibition at analgesic doses. Here, we report cryo-EM structures of human GlyT2 bound to the potent pseudo-irreversible inhibitor ORG25543, a reversible analogue RPI-GLYT2-82, and in substrate-free state. Both inhibitors bind an extracellular allosteric site, locking the transporter in an outward-open conformation, whereas the substrate-free GlyT2 adopts an inward-open conformation. We demonstrate that RPI-GLYT2-82 has a faster off-rate, providing analgesia in mouse neuropathic pain models, with no observed mechanism-based side-effects or addiction liability. Our data provide a model for allosteric inhibition, enabling structure-based design of new non-opioid analgesics.

Keywords: glycine transporter 2; allosteric inhibition; neuropathic pain; analgesics; non-opioids; SLC6A5

INTRODUCTION

Only one in four patients with neuropathic pain respond to the current gold standard treatment, pregabalin, and even then, its efficacy is limited and accompanied by dose-dependent side effects[1,2]. The dearth of effective therapeutics for chronic pain has led to an overreliance on opioid medications, exacerbating opioid use disorder and its associated mortality[1]. There is an urgent need for the development of safe and effective analgesics that circumvent the opioid pathway and selectively target new mechanisms to overcome limitations in existing treatments.

A key adaptive feature of neuropathic pain is a reduction in inhibitory glycinergic neurotransmission in the dorsal horn of the spinal cord, which impairs the capacity to distinguish between nociceptive (painful) and harmless stimuli[3]. At glycinergic synapses, glycine is an inhibitory neurotransmitter that activates post-synaptic glycine receptors. Glycine homeostasis is tightly regulated by the glycine-selective transporters GlyT1 and GlyT2 throughout the central nervous system (CNS). GlyT1 (encoded by *SLC6A9*) is expressed at both excitatory and inhibitory synapses, while GlyT2 (encoded by *SLC6A5*) is exclusively localised to presynaptic neurons of inhibitory synapses[4]. GlyT2 has a key role in regulating extracellular glycine concentrations to control glycine receptor activity, and in recycling synaptic glycine into presynaptic neurons to maintain glycinergic neurotransmission[5-9]. The clear role of GlyT2 in aberrant pain signalling, along with its relatively restricted distribution in the spinal cord, makes GlyT2 an attractive target for neuropathic pain therapeutics.

Restoration of inhibitory glycinergic signalling by pharmacological inhibition of GlyT2 alleviates pain in several preclinical models[10-15]. ORG25543 is a potent, pseudo-irreversible, and non-competitive[16] inhibitor of GlyT2 that is analgesic in animal models of neuropathic pain[10,14,17,18]. ORG25543, however, did not progress to clinical use due to its significant on-target side effects, recapitulating the mouse *GlyT2*$^{-/-}$ knockout (KO) phenotype, including tremors, seizures, and even mortality at the maximal analgesic dose, attributed to its high affinity and slow off-rate[10,14]. In contrast, siRNA knockdown of GlyT2 to 30% of wild type levels and acute and chronic dosing of GlyT2 inhibitor tool compounds, results in prolonged analgesia in mouse models of neuropathic pain without side effects[12]. The endogenous bioactive lipid N-arachidonoyl glycine and its synthetic derivatives including oleoyl-D-lysine (ODLys) cause partial inhibition of GlyT2 comparable to knockdown studies and provide analgesia in animal models of pain without side effects, however, the poor pharmacokinetics prevented progression of the bioactive lipids to clinical trials[19,11,10]. Recently, an ORG25543-based benzamide chemotype GlyT2 inhibitor, opiranserin (VVZ-149), has reached a confirmatory phase 3 trial of laparoscopic colectomy for treating postoperative pain and reducing opioid consumption[20,21].

GlyT2 belongs to the secondary active neurotransmitter/sodium symporters (NSSs) of the solute carrier 6 (SLC6) family of transporters[22,23]. NSSs operate via an alternating access mechanism, where conformational rearrangements of transmembrane helices during the transport cycle expose the substrate-binding site alternately to either side of the membrane. Binding and occlusion of the extracellular substrate is dependent on a Na^+ (and Cl^- in eukaryotic NSSs) gradient, with GlyT2 co-transporting three Na^+ ions and one Cl^- ion with glycine[24, 25-27]. Upon binding, the transporter transitions from an outward-facing to an inward-facing confirmation followed by intracellular opening and release of bound ions and substrate. Several competitive and non-competitive inhibitors of SLC6 transporters that target the outward- or inward-facing conformations of the transporters have been developed[28-40]. Competitive and non-competitive inhibitors of GlyT2 create distinct glycine concentration dynamics[9]. Competitive inhibitors should be largely ineffective at the high synaptic glycine concentrations required for synaptic transmission, whereas non-competitive inhibitors will function in a fundamentally different manner and will enable effective targeting of GlyT2 in neurological disorders. Targeting an allosteric site offers greater opportunities for selectivity as orthosteric sites are less divergent in their amino acid compositions. Further, since glycine is the only known substrate transported by GlyT2, the chemical space that can be explored for orthosteric inhibition is restricted[41].

Here we present, to our knowledge, the first structures of human GlyT2 bound to ORG25543 (4-(benzyloxy)-N-{[1-(dimethylamino)cyclopentyl]methyl}-3,5-dimethoxybenzamide), a newly synthesized lower affinity analogue of ORG25543, RPI-GLYT2-82 (1-benzoyl-N-((4-(dimethylamino)tetrahydro-2H-pyran-4-yl)methyl)indoline-5-carboxamide), and in the substrate-free state. We capture the inhibitor-bound structures in the outward-open state and the substrate-free structure in an inward-open conformation. We show that RPI-GLYT2-82 is efficacious at alleviating allodynia in both chronic constriction injury (CCI) and partial sciatic nerve ligation (PSNL) mouse models with no observed side effects at the maximal analgesic dose of the inhibitor. Our study reveals the molecular determinants and mechanism of allosteric inhibition of glycine transport.

RESULTS

RPI-GLYT2-82 is a novel, non-competitive GlyT2 inhibitor

We have developed a lower affinity non-competitive analogue of ORG25543, RPI-GLYT-82, with the objective of identifying an allosteric inhibitor that provides analgesia without side effects (Figure 1A, see Methods S1). Indicative of high-affinity binding, we measured a half-maximal inhibitory concentration (IC_{50}) for ORG25543 of 11.4 nM (95% CI: 8.0 to 16.4 nM) on wild-type GlyT2 ($GlyT2^{WT}$), whereas RPI-GLYT2-82 showed lower affinity with an IC_{50} of 554 nM (95% CI: 412 to 747 nM) (Figures 1B and 1C).

ORG25543 is an early GlyT2 inhibitor and a widely used tool compound, however, a narrow therapeutic index between minimally effective and maximally tolerated doses have been observed for the compound, with noted adverse effects. This profile has been attributed to slow off-rate binding kinetics of ORG25543, and it has been hypothesized that improving the reversibility of ORG25543-based compounds could potentially decrease the on-target side effect profile[14]. Indeed, drugs with fast off-rates and short residence times have been reported to be advantageous for targets that pose a potential risk for mechanism-based toxicity[42,43]. RPI-GLYT2-82 exhibits markedly faster off-rate binding kinetics, with complete restoration of pre-inhibitor glycinergic-induced currents of $GlyT2^{WT}$ within 5 minutes (Figure 1D). This contrasts with ORG25543, where $GlyT2^{WT}$ current restores to only 12.5% (SD= 4.8%) of pre-inhibitor conditions at 30 minutes (Figure 1E).

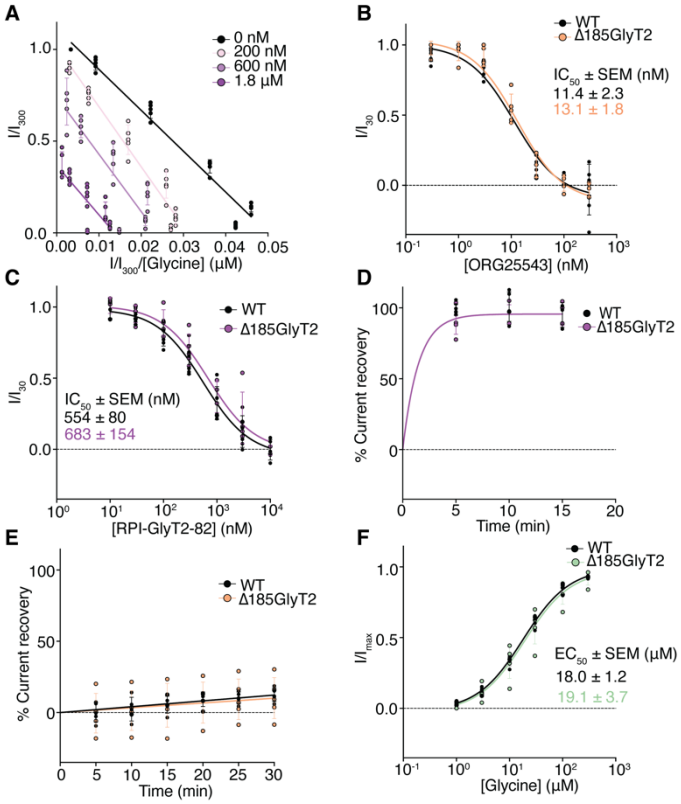

Figure 1. RPI-GLYT2-82 is a non-competitive inhibitor of GlyT2.
(A) Eadie-Hofstee transformation of glycine-dependent currents in the presence of different concentrations of RPI-GLYT2-82 showing the non-competitive behaviour of the inhibitor. Data were analysed using nonlinear regression (see Methods). (B) ORG25543 dose-response normalised to pre-inhibitor currents induced by 30 μM glycine. (C) RPI-GLYT2-82 dose-response normalised to pre-inhibitor currents induced by 30 μM glycine. (D) RPI-GLYT2-82 is reversible and completely washes out within 5-minutes. (E) ORG25543 has prolonged effects with minimal restoration of glycine-induced currents 30-minutes post ORG25543 exposure. Results are normalised to pre-inhibitor glycine-induced currents (%). (F) Normalised glycine-dependent transport currents in $GlyT2^{WT}$ and $GlyT2^{\Delta 185}$ expressing *Xenopus laevis* oocytes showing comparable transport activity between the two constructs. EC_{50}, IC_{50}, washout and competition experiments (A–F) were performed with $n = 5$ biological replicates with error bars representing the standard deviation.

Given the lack of detailed experimental information on the location of the binding site occupied by ORG25543 and RPI-GLYT2-82 and to understand the mechanism underlying the reversibility of the compounds, we next sought to determine the structures of GlyT2 bound to inhibitors.

Overall architecture of human GlyT2

The N terminus of human GlyT2 is predicted to be largely unstructured and its deletion does not affect trafficking of GlyT2 to the plasma membrane or the K_M for glycine transport[44]. To facilitate expression and purification of GlyT2, we truncated residues 2-185 of the N terminus of GlyT2 yielding the $GlyT2^{\Delta 185}$ construct. $GlyT2^{\Delta 185}$ exhibits a similar EC_{50} value for glycine transport compared to the full-length, wild-type transporter ($GlyT2^{WT}$) (Figure 1F). Further, both ORG25543 and RPI-GLYT2-82 exhibit similar IC_{50} values at $GlyT2^{\Delta 185}$ compared to $GlyT2^{WT}$ (Figures 1B and 1C).
We purified $GlyT2^{\Delta 185}$ in a mixed lauryl maltose neopentyl glycol (LMNG), glyco-diosgenin (GDN), and cholesteryl hemisuccinate (CHS) micelle (1.0:1.0:0.1 LMNG:GDN:CHS), obtaining monodisperse and homogenous $GlyT2^{\Delta 185}$ (Data S1) for cryo-electron microscopy (cryo-EM) studies. We determined the structures of $GlyT2^{\Delta 185}$ bound to inhibitors ORG25543, or RPI-GLYT2-82, or in substrate-free state at 2.49 Å, 2.79 Å, and 2.97 Å resolution, respectively (Figures 2A-2F, Data S1).
The high-quality of the resulting density maps enabled us to unambiguously model all transmembrane (TM) helices, with TMs 1 and 6 unwinding approximately halfway across the membrane, a characteristic for the substrate binding site in SLC6 transporters, intracellular and extracellular loops except parts of extracellular loop 2 (EL2) due to its high degree of flexibility (Figure 2, Data S1), and the positioning of bound ligands, Cl^- and Na^+ ions, as well as multiple cholesterol and CHS molecules. The conserved disulfide bridge formed between C311 and C320 (EL2) is observed in all three structures (Data S1, Figure S1). GlyT2 adopts the expected architecture of SLC6 transporters, comprising 12 α-helical TMs in an inverted pseudo-twofold symmetric organisation of TMs 1–5 relative to TMs 6–10, denoted as the LeuT fold[45] (Figure 2, Data S1).

Non-competitive inhibitors lock GlyT2 in outward-open conformation

The inhibitors capture the transporter in an outward-open conformational state, where the central substrate site is accessible to the solvent via the extracellular vestibule. The Cα-Cα distance between the two conserved extracellular gating residues, R216 on TM1b and D633 on TM10, is 13.9 Å in both the ORG25543- and RPI-GLYT2-82-bound structures of $GlyT2^{\Delta 185}$, consistent with previous outward-facing NSS structures[32,33]. The cytoplasmic pathway is closed, with TM1a residing within the protein core, where the conserved residue W194 (TM1a) plugs a hydrophobic pocket characteristic of a closed intracellular pathway (Figure 2, Figures S1 and S2).

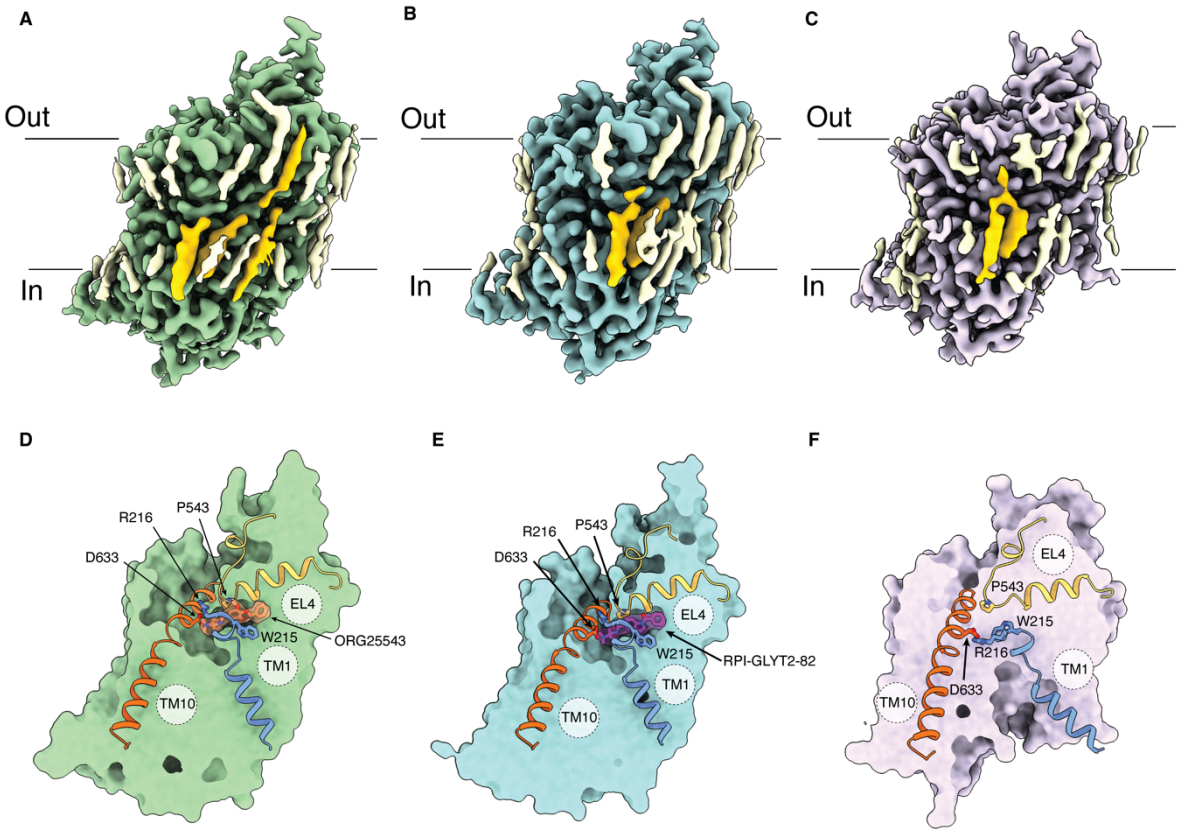

Figure 2. Outward-open inhibitor-bound and inward-open substrate-free states of GlyT2. Cryo-EM density maps of GlyT2$^{\Delta 185}$ bound to (A) ORG25543 (green map contour level = 0.055 in ChimeraX) (B) RPI-GLYT2-82 (blue map contour level = 0.038 in ChimeraX) and (C), in the substrate-free form (pink map contour level = 0.04 in ChimeraX). Lipid densities are shown in light yellow, and densities corresponding to sterols built into the models are shown in dark yellow. (D), (E), (F), Surface representation of the inhibitor-bound and substrate-free structures of GlyT2$^{\Delta 185}$, viewed parallel to the membrane. (D) Slice view of GlyT2$^{\Delta 185}$ showing the ORG25543 binding pocket (orange, compound density shown at map contour level = 0.055 in ChimeraX). (E) Slice view of GlyT2$^{\Delta 185}$ showing the RPI-GLYT2-82 binding pocket (dark purple, compound density shown at map contour level = 0.038 in ChimeraX). (F) Slice view of GlyT2$^{\Delta 185}$ in the substrate-free form. The closed extracellular vestibule around W215 (blue) and the open intracellular pathway are displayed. Residues W215 (TM1 – blue), R216 (TM1 – blue), P543 (EL4 – yellow), D633 (TM10 – orange) are shown as sticks in (D), (E), (F). See also Data S1.

In both inhibitor-bound structures of GlyT2, we observe a clear density for a Cl^- ion that is coordinated by the residues Y233 (TM2), Q473 (TM6a), S477 (TM 6a) and S513 (TM7) (with mean coordination distance of 2.8 Å ± 0.4 and 2.9 Å ± 0.5 in ORG25543- and RPI-GLYT2-82-bound structures of GlyT2$^{\Delta 185}$, respectively) (Figures 3A and 3B). We do not, however, observe any densities for sodium ions at Na2 or the proposed Na3 sites[25,27]. This is unsurprising given that ORG25543 binding has been reported as sodium-independent[16], and similarly, RPI-GLYT2-82 binding is also likely independent of Na^+. We observe a clear non-protein density (a prominent 9.7 r.m.s.d. signal) where a Na^+ ion in the Na1 site would bind (Figures 3A and 3B). We initially assigned a water molecule to this density as one of the main coordinating residues, N213 (TM1b), rotates away from the Na1 site to interact with the respective inhibitor in both ORG25543- and RPI-GLYT2-82-bound structures of GlyT2$^{\Delta 185}$ (Figures 3 and 4). During our molecular dynamics (MD) simulations, we modelled the protein complex with the Na1 site occupied by water in the starting conformation, however extracellular Na^+ ions spontaneously bound to the Na1 site in four out of six replicate simulations, and the site remained occupied by Na^+ across 50% of the 3000 ns combined replicate simulations (Figure S3, Table S1). We therefore modelled a Na^+ ion at the density at the Na1 site, coordinated by the backbone carbonyl oxygens of A208 (TM1) and S477 (TM6),

and a water molecule reminiscent of a loosely bound hydrated Na^+ exposed to the extracellular space (Figures 3A and 3B, Figure S3).

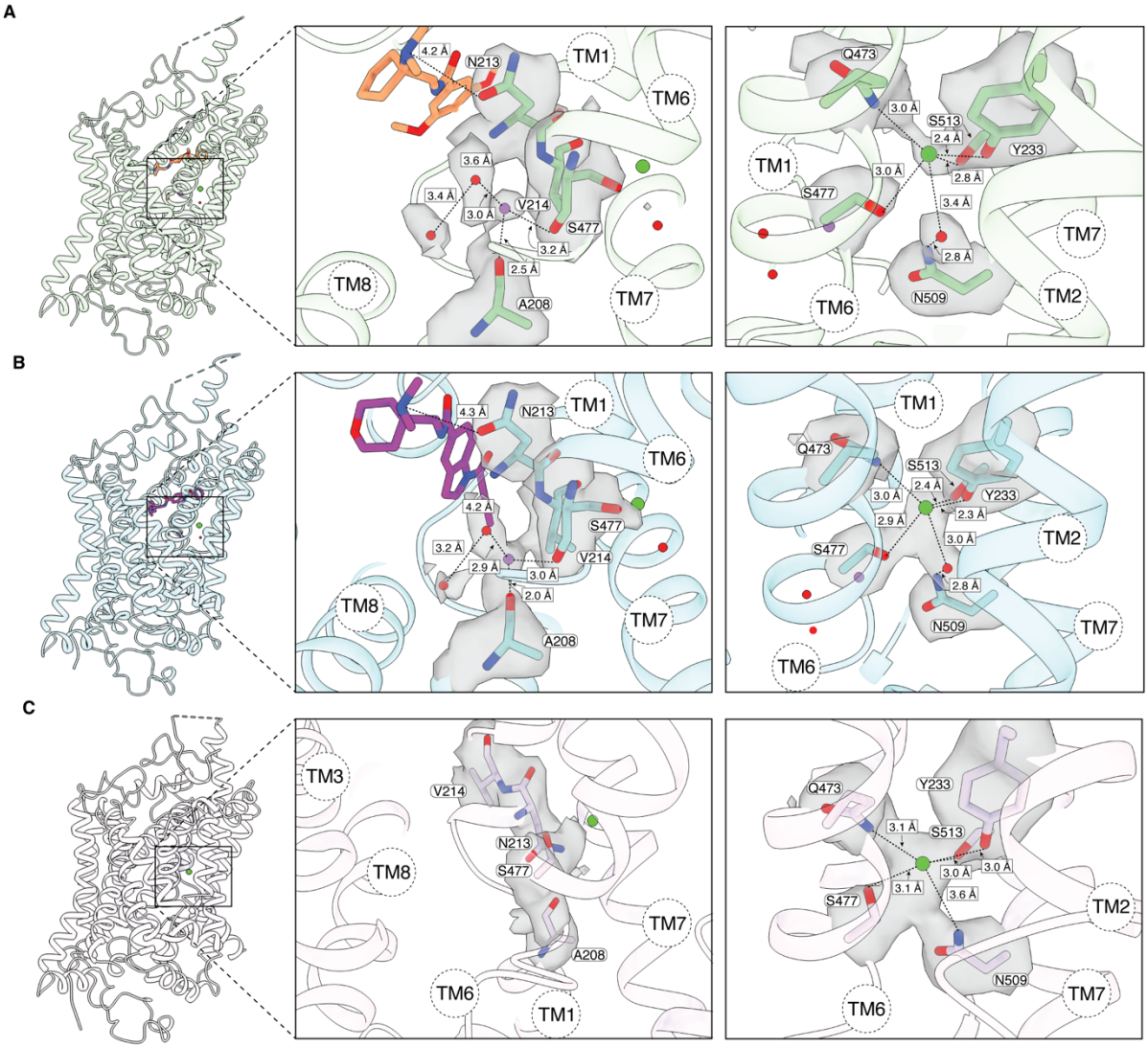

Figure 3. Architecture and ion binding sites of GlyT2$^{\Delta 185}$.
(A) Cartoon representation of ORG25543-bound GlyT2$^{\Delta 185}$. Left zoom in is of the Na^+ ion (purple) modelled into the density at Na1 with coordination residues (contour level = 0.050 in ChimeraX). ORG25543 is shown in orange and water molecules are shown in red (with corresponding densities). Right zoom in is of the Cl^- ion (green) modelled in ORG25543-bound GlyT2$^{\Delta 185}$ with coordinating residues (mean coordination distance of 2.8 Å ± 0.4) and densities shown (contour level = 0.050 in ChimeraX). (B) Cartoon representation of RPI-GLYT2-82-bound GlyT2$^{\Delta 185}$. Left zoom in is of the Na^+ ion (purple) modelled into the density at Na1 site with coordination residues (contour level = 0.045 in ChimeraX). RPI-GLYT2-82 is shown in magenta and water molecules are shown in red (with corresponding densities). Cl^- ion (green) modelled in RPI-GLYT2-82-bound GlyT2$^{\Delta 185}$ with coordinating residues (mean coordination distance of 2.9 Å ± 0.5) and densities shown (contour level = 0.045 in ChimeraX). (C) Cartoon representation of substrate-free GlyT2$^{\Delta 185}$. Left zoom in is of the collapsed Na1 site with otherwise Na1 site forming residues shown with corresponding densities (contour level = 0.030 in ChimeraX). Right zoom in is of the Cl^- ion (green) modelled in substrate-free GlyT2$^{\Delta 185}$ to a density with coordinating residues (mean coordination distance of 3.1 Å ± 0.3) and densities shown (contour level = 0.030 in ChimeraX). See also Figure S3 and Table S1.

ORG25543 and RPI-GLYT2-82 wedge in an allosteric site

The cryo-EM densities of ORG25543 and RPI-GLYT2-82 were of high quality allowing unambiguous assignment of the respective poses (Figures 4A and 4B). We modelled the

inhibitors in an allosteric pocket sandwiched in between TM1b, TM10, and EL4 (Figures 4C and 4D). This pocket is lined with predominantly hydrophobic residues from TMs 1, 3, 5, 7, 8, 10 and EL4.

The scaffold of ORG25543 and RPI-GLYT2-82 can be divided into four key substituents (R_1 – R_4) (Figures 4E and 4F). These substituents, in ORG25543 and RPI-GLYT2-82, respectively, are: (R_1) the central benzamide phenyl ring, and the central indoline, (R_2) benzyloxy, and benzoyl phenyl rings, (R_3) cyclopentyl and tetrahydropyran rings, and (R_4) the pendant ammonium present in both compounds. The central R_1 group of the inhibitors is stacked between W215 (TM1b) and P543 (EL4). The distal R_2 ring of the inhibitors is caged by a network of residues including W215 (TM1b), I520 (TM7), Y550 (EL4) and F567 (TM8), as well as A546 (EL4) and M570 (TM8). The pocket harbouring the R_3 substituents is relatively large and exposed to solvent, with hydrophobic residues I290 (TM3), P543 (EL4), and F629 (TM10) contributing to the stabilisation of the R_3 group.

The conserved residues R216 (TM1b) and D633 (TM10) that form the extracellular molecular gate in NSS through a salt bridge, are engaged in hydrogen bond and salt bridge interactions with the inhibitor in both ORG25543- and RPI-GLYT2-82-bound structures of GlyT2$^{\Delta 185}$ (Figures 4C and 4D), with pendant ammonium (R_4) of inhibitors forming a charged-reinforced hydrogen bond and a salt bridge with D633, and the carbonyl oxygen of R_1 forming a hydrogen bond with the side chain of R216. The allosteric inhibitor binding site on GlyT2 resembles that of MRS7292-bound dopamine transporter (DAT)[35], suggesting a common allosteric regulatory site in SLC6 transporters (Figure S4).

MD-based r.m.s.d. analysis confirmed stable binding of ORG25543 at the allosteric site for 95.4% of combined simulation replicas. The central benzamide phenyl ring (R_1) showed minimal fluctuation, stabilized by TM1b, EL4, and TM8 (Figure S5, Table S2), while the distal benzyloxy phenyl substituent (R_2) and the solvated pendant ammonium (R_4) had greater mobility (Figure S6). R_2 frequently interacted with residues of the cryo-EM pocket for this substituent (Table S2). Despite its higher fluctuations, R_3 remained in a hydrophobic cavity flanked by Y286 and Y287 on TM3 (Figure S7). Hydrogen bond analysis indicated stable interactions between the benzamide of ORG25543 and L211 and intermittent interactions with R216, while the ORG25543 protonated amine (R_4) is intermittently engaged in a charged-reinforced hydrogen bond with D633 as observed with the pose in cryo-EM structure of GlyT2$^{\Delta 185}$ (Figure S7, Table S2). The probability density map showing the relative likelihood of bound GlyT2 ligand positions (Figure S7), demonstrates that ORG25543 resides in a deep energetic minimum at the allosteric binding site, with an occupancy of 95%.

In comparison, RPI-GLYT2-82, adopts a less stable binding pose than ORG25543, exhibiting higher positional fluctuations within the first 50 ns of simulations. It remains in the binding site for only 48% of the combined simulation replicas and moves towards the central substrate binding site for the remaining time (Figure S7). Like ORG25543, the distal benzoyl phenyl ring (R_2), tetrahydropyran (R_3), and pendant ammonium (R_4) of RPI-GLYT2-82 had the greatest positional fluctuations, while the central indoline (R_1) formed contacts with the same set of residues coordinating the ORG25543 R_1 moiety in the GlyT2 allosteric site (Figure S7, Table S2).

We used endpoint free energy methods[46-48] to analyse MD simulation trajectories of GlyT2-bound complexes. Binding enthalpy decomposition revealed that L211, W215, and D633 contributed significantly to ORG25543 binding (Figure S7), while there was a 0.83–0.92-fold reduction in binding enthalpy for RPI-GLYT2-82 (95% C.I.) (Figure S7). The per-residue energy decompositions suggest the lower experimental IC_{50} value for RPI-GLYT2-82 stems from altered interaction enthalpy with L211, R216, and P543 (Figure S7).

RPI-GLYT2-82 binding to GlyT2 is reversible

Testament to the critical role of W215 in accommodating the R_1 and R_2 substituents of the inhibitors, the conservative mutation to phenylalanine results in a ~ three-fold decrease in potency of ORG25543 (IC_{50} at GlyT2^{WT}= 11.4 nM, GlyT2^{W215F} = 32.2 nM) (Figure 4G). Interestingly, whilst this mutation has mild effects on the potency, it significantly increases the rate of ORG25543 washout (Figure 4H), similar to the previously characterised Y550L

mutation[18]. Introducing the D633E point mutation significantly reduces the potency of ORG25543 (~ 14-fold) and results in complete washout within 5 minutes (Figures 4G and 4H) highlighting the critical role of this interaction for potency of the inhibitor.
Both ORG25543 and RPI-GLYT2-82 have a pendant phenyl ring (R_2) that snorkels deep into the binding pocket and is engaged in edge-to-face $\pi-\pi$ interactions with W215 (TM1b) and Y550 (EL4). The R_2 group is positioned orthogonally to the core (R_1) of both inhibitors, benzamide phenyl ring in ORG25543 and indoline in RPI-GLYT2-82. As a benzamide, the pendant benzoyl phenyl ring of RPI-GLYT2-82 is likely to adopt a lower energy coplanar orientation with the carbonyl to which it is attached, reducing conformational flexibility. However, in its binding pose in the allosteric pocket, this pendant phenyl ring must twist nearly 90 degrees to adopt the bioactive orthogonal orientation, which likely induces torsional strain and is energetically unfavourable[49]. Further, the indoline benzamide carbonyl oxygen of RPI-GLYT2-82 points toward a non-polar pocket (Figure 4D), which is likely to contribute to destabilizing contacts.
Moreover, the R_3 substituent is a small hydrophobic cyclopentane ring in ORG25543, residing in a hydrophobic pocket (Figure 4). The smaller and more lipophilic cyclopentane of ORG25543 is likely able to easily fit in this pocket, potentially displacing any resident waters and interacting via various van der Waals binding interactions. However, the RPI-GLYT2-82 tetrahydropyran moiety (R_3) is larger and more polar than the ORG245543 cyclopentane ring, and its oxygen atom is not engaged in any significant binding interactions within the hydrophobic R_3 pocket (Figure 4). The increased size of the tetrahydropyran ring coupled with a potential lack of significant binding interactions with the polar tetrahydropyran oxygen may better enable solvent water to “dissolve” the ring out of this hydrophobic binding. The increased size and polarity of R_3 is another likely factor to explain the lower potency and improved washout kinetics of RPI-GLYT2-82 compared to ORG25543.

Substrate-free state

Despite the addition of the GlyT2 inhibitor oleoyl-D-lysine throughout the purification, we were not able to observe any density corresponding to the inhibitor. The low solubility of the compound likely contributed to its inability to bind effectively or remain in sufficient concentration in solution for binding. We therefore present this structure as a substrate-free state of GlyT2$^{\Delta 185}$, which is captured in an inward-open conformation at 2.97 Å resolution (Figure 2C, Data S1).
The extracellular gate residues, R216 and D633 form a salt bridge precluding solvent access from the extracellular side[28]. The intracellular side of GlyT2 has a large open cavity, facilitated by solvation of TM5 and protrusion of TM1 into the micelle. The intracellular part of TM5 is unwound, right before the conserved helix-breaking Gly(X_9)Pro motif (Gly419(X_9)Pro429 in GlyT2), a feature that creates a solvent pathway that provides water access from the cytoplasm to the Na2 site[50]. The N-terminal segment of TM1 (TM1a) is bent away from the core of GlyT2, opening the release pathway into the intracellular side. The splayed motion of TM1 disrupts the interaction between the TM1a and the hydrophobic patch at the cytoplasmic part of GlyT2$^{\Delta 185}$ that is otherwise present in outward-open conformations of GlyT2$^{\Delta 185}$ and other outward-facing or inward-occluded structures of NSS[32,51,52] (Figure 2F, Figure S2).
We observe a clear density for a Cl^- ion in the cryo-EM map of the substrate-free structure of GlyT2$^{\Delta 185}$. The Cl^- ion coordination is slightly different to that of inhibitor-bound outward-open structures of GlyT2$^{\Delta 185}$. While Cl^- ion is coordinated by the same conserved residues Y233 (TM2), Q473 (TM6a), S477 (unwound region of TM6a) and S513 (TM7), it is also coordinated by N509 on TM7 (mean coordination distance of 3.2 Å ± 0.2). In outward-open structures of GlyT2, the Cl^- ion interacts indirectly with N509 through a water molecule (Figure 3C). We do not, however, observe any densities for sodium ions at Na1, Na2 or the proposed Na3 sites, consistent with an inward-open conformational state of the transporter[30,52] (Figure 3C).

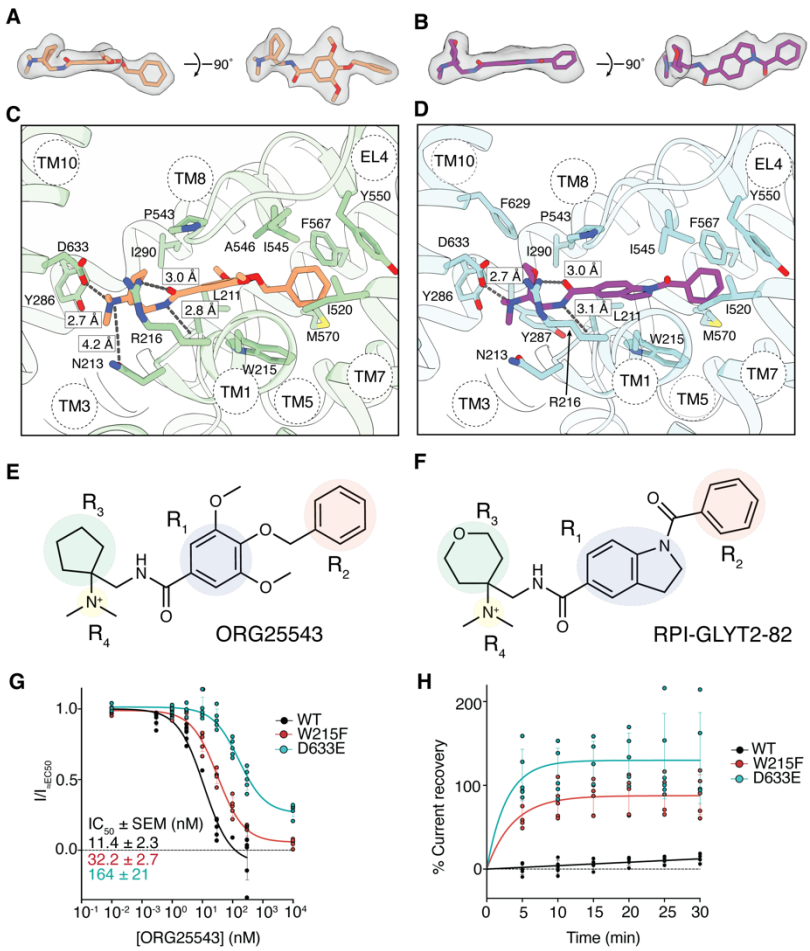

Figure 4. ORG25543 and RPI-GLYT2-82 bind to an allosteric pocket. (A) Cryo-EM density of ORG25543 (map contour level = 0.055 in ChimeraX). (B) Cryo-EM density of RPI-GLYT2-82 (map contour level = 0.04 in ChimeraX). (C) ORG25543 (orange) bound to GlyT2$^{\Delta 185}$ (green). Interacting residues shown as sticks and H-bonds and ionic interactions shown as grey dashed lines. N213 is likely involved in a weak hydrogen bond interaction with the polarised C–H of the methyl group attached to positively charged ammonium nitrogen of R_4 substituent. (D) RPI-GLYT2-82 (purple) bound to GlyT2$^{\Delta 185}$ (blue). Interacting residues shown as sticks and H-bonds and ionic interactions shown as grey dashed lines. (E) Chemical structure of ORG25543 and key chemical substituents R_1 (blue), R_2 (orange), R_3 (green) and R_4 (yellow) outlined. (F) Chemical structure of RPI-GLYT2-82 and key chemical substituents (R_1–R_4) outlined. (G) ORG25543 dose-response curves of wild-type GlyT2 and mutants W215F (red) and D633E (blue). Data normalised to pre-inhibitor currents induced by glycine. (H) Reversibility of ORG25543 on GlyT2^{WT} and GlyT2^{W215F} and GlyT2^{D633E} mutants. Experiments for (G) and (H) were performed with $n = 5$ biological replicates with error bars representing the standard deviation.

Cholesterol binding sites

The activity of GlyT2 and related SLC6 transporters is modulated by cholesterol[18,53-60]. We have accordingly identified several density features consistent with cholesterol (CHOL) or CHS molecules (Figure 5).

In all three structures of GlyT2$^{\Delta 185}$, we observed a density feature that accommodates a cholesterol molecule on the inner leaflet in a pocket formed by TM2, TM7 and TM11, equivalent to previously reported CHOL2[32,35,36] (Figure 5A). We identified an additional density that neighbours the CHOL2 site, where we modelled a CHS molecule (CHOL5). These two molecules form hydrogen bonds with N674 (IL5). Notably, while the cholesterol at the CHOL2 site appears to be conserved, the asparagine residue is not conserved across the NSS family. In dDAT and serotonin transporter (hSERT) it is a glycine residue, in hDAT a serine, and in hGlyT1 and LeuT a proline residue (Figure 5A, Figure S1).

We also observe a density adjacent to but distinct from the previously reported CHOL1 site[34,36], where we modelled a CHS molecule (CHOL6). Unlike CHOL1, this site does not involve interactions with TM5 but rather lies parallel to and interacts with TM7. Above CHOL6, we identified a novel sterol site (CHOL7), formed by TM5, TM7 and EL4, where we modelled a cholesterol molecule (Figure 5A). A lipid density was observed in a recent DAT structure[35] at the sites overlapping with both CHOL6 and CHOL7 in GlyT2$^{\Delta 185}$. We further modelled a cholesterol molecule into a site that partially overlaps with CHOL3, and with the CHOL5 site proposed in molecular dynamics simulations of dDAT (named CHOL3' in GlyT2) [32,33,61]. Interestingly, this cholesterol is embedded within the protein, in contrast to its positioning in other SLC6 structures, where it aligns with the membrane. This cholesterol molecule resides in a site formed by TMs 3, 9, 10 and 12, characterised by a high density of methionine residues (Figures 5B and 5C). This density feature is consistently present in all three conformational states, suggesting it may act as an important stabilising element of GlyT2. We do not observe clear cholesterol-like densities at CHOL1 or CHOL4 sites[32].

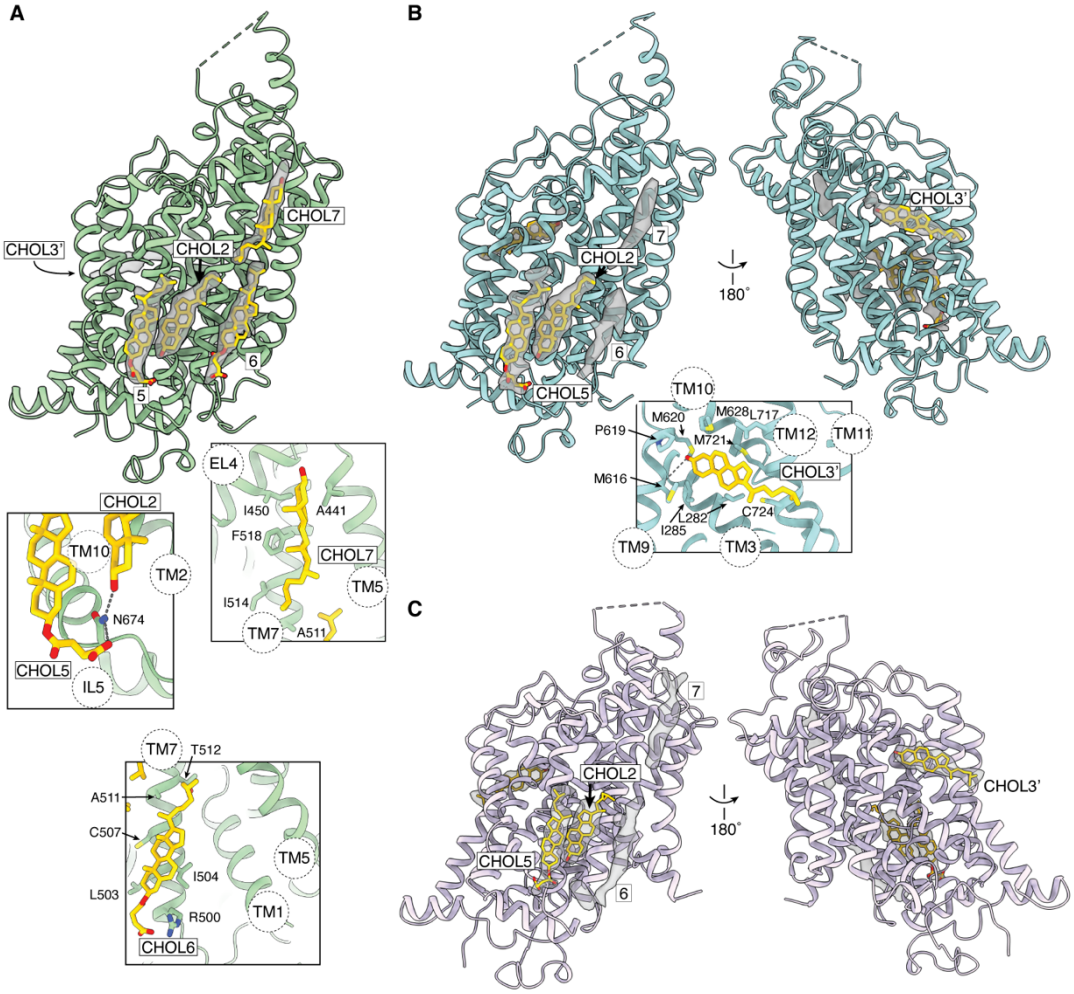

Figure 5. Novel and conserved sterols bound to GlyT2. (A) Two cholesterol molecules (CHOL2 and CHOL7) and two CHS molecules (CHOL5 and CHOL6) were modelled (yellow sticks) into non-protein densities (grey) in ORG25543-bound GlyT2$^{\Delta 185}$ (map contour level = 0.055 in ChimeraX). The CHS molecule at site 6 is positioned adjacent to the conserved CHOL1 but occupies a distinct location and does not interact with TM5. (B) Sterols were modelled into CHOL2 (cholesterol), CHOL5 (CHS) and CHOL3' (cholesterol) (yellow sticks) sites of RPI-GLYT2-82-bound GlyT2$^{\Delta 185}$. Densities for sites 6 and 7 are shown but the corresponding sterols were not modelled in this structure (map contour level = 0.038 in ChimeraX). Hydrogen bonds are shown as grey dashed lines. (C) Sterols were modelled into CHOL2 (cholesterol), CHOL5 (CHS) and CHOL3' (cholesterol) in substrate-free GlyT2$^{\Delta 185}$. Densities are also shown for sites 6 and 7 but the corresponding sterols were not modelled in the structure (map contour level = 0.04 in ChimeraX).

RPI-GLYT2-82 is anti-allodynic in mouse models of neuropathic pain

In previous studies, intraperitoneal (i.p.) administration of ORG25543 reduced mechanical allodynia in the CCI mouse model at 30 and 50 mg/kg from 30 minutes post-injection until 6 hours, with peak effects between 1 and 2 hours[10]. At 50 mg/kg, ORG25543 caused a reversal of allodynia, however, this coincided with confounding seizures and one lethality[10]. Furthermore, a dose of 50 mg/kg ORG25543 caused a near-complete loss of baseline rotarod performance across the first hour post-injection[10]. These significant side effects demonstrate the need for developing alternative GlyT2 inhibitors and tool compounds.

We first conducted mouse pharmacokinetic (PK) profiling of RPI-GLYT2-82 via i.p. administration to determine PK parameters, and then we conducted a separate in-life CNS PK study to assess total brain (C_b) and plasma (C_p) concentrations at 30 and 120 minutes (Data S2). We then calculated unbound drug exposures in plasma ($C_{u,p}$) and brain ($C_{u,b}$) at these timepoints using *in vitro* data for mouse plasma protein binding (%PPB, 21.0% unbound) and brain tissue homogenate binding (6.3% unbound), respectively (Data S2). RPI-GLYT2-82 exhibited suitable PK characteristics for further proof-of-concept analgesic assessment, achieving a $C_{b,u}$ of 597.89 nM at 30 minutes at a 50 mg/kg i.p. dose (Table S3). The observed $C_{b,u}$ at 30 minutes is approximately equal to the GlyT2 IC_{50} for the compound (Figure 1C, Table S3).

We tested RPI-GLYT2-82 as an analgesic in the CCI and PSNL mouse models of neuropathic pain, comparing its efficacy to the current gold standard neuropathic pain drug, pregabalin, as well as to previously published effects of ORG25543[10]. We assessed the analgesic efficacy of RPI-GLYT2-82 by measuring mechanical allodynia in mice upon i.p. administration. We observed dose-dependent anti-allodynia at the 50 and 100 mg/kg doses, with maximum efficacy between 90 minutes and 3 hours post-administration in both the CCI and PSNL models (Figure 6).

Importantly, the adverse neuromotor effects of ORG25543 were not observed with analgesic doses of RPI-GLYT2-82 during the treatment period (Figure 6A). Furthermore, the 50 mg/kg analgesic dose of RPI-GLYT2-82 did not cause changes in respiration frequency, minute volume (MVb), and tidal volume (TVb) using whole-body plethysmography in mice (Figures 6E-6G). However, a dose five-fold higher than the minimally analgesic dose (250 mg/kg, i.p.) produced an initial 61% reduction in baseline performance, which rebounded over the 90-minute time-course. This effect coincided with transient sedation, which was most apparent in the first 15–30 minutes and then wearing off entirely with complete recovery at 90 minutes (Figures 6B and 6C). The 250 mg/kg dose caused transient changes in respiratory frequency and MVb in the first hour, and TVb in the first 30 minutes (Figures 6E-6G). These transient effects may also result from sedation observed for this dose (Figure 6C).

Collectively, the *in vivo* analgesic and side effect data for RPI-GLYT2-82 provide evidence that the compound produces statistically significant dose-dependent analgesia without the adverse neuromotor effects associated with ORG25543 and the *GlyT2*$^{-/-}$ KO mouse (e.g., tremors, convulsions, and spasticity)[10,12]. Whilst GlyT2 is the primary target of RPI-GLYT2-82 (IC_{50} = 554 nM, Figure 1C), it is also an antagonist at the serotonin 2A (5-HT2A) receptor (IC_{50} = 1.9 μM), suppressing the transmission of pain signals by both GlyT2 and 5-HT2A receptor to induce analgesia. Notably, antagonist activity at 5-HT2A has been previously reported for other GlyT2 inhibitors of the ORG25543 class, including opiranserin[21,62]. RPI-GLYT2-82 also exhibits appreciable inhibitory activity at the serotonin transporter (SERT, IC_{50} = 4.7 μM), but is inactive at other off-targets screened within the Cerep panel that are known to promote sedation (i.e., γ-aminobutyric acid type A ($GABA_A$), histamine (H1), adenosine, adrenergic, and muscarinic receptors) (Data S2).

The rewarding properties of opioids limit their clinical usefulness due to the risk of opioid use disorder. To assess the rewarding properties of RPI-GLYT2-82, we compared its ability to induce preference in a conditioned place preference (CPP) paradigm for morphine. Morphine (10 mg/kg, i.p.) treated mice exhibited a significant increase in preference for the paired chamber ($p = 0.0287$) whereas RPI-GLYT2-82 (50 and 150 mg/kg, i.p.) treated mice did not

show significant changes in preference (Figure 6H), holding promise as a foundation for the development of non-addictive pain medications.

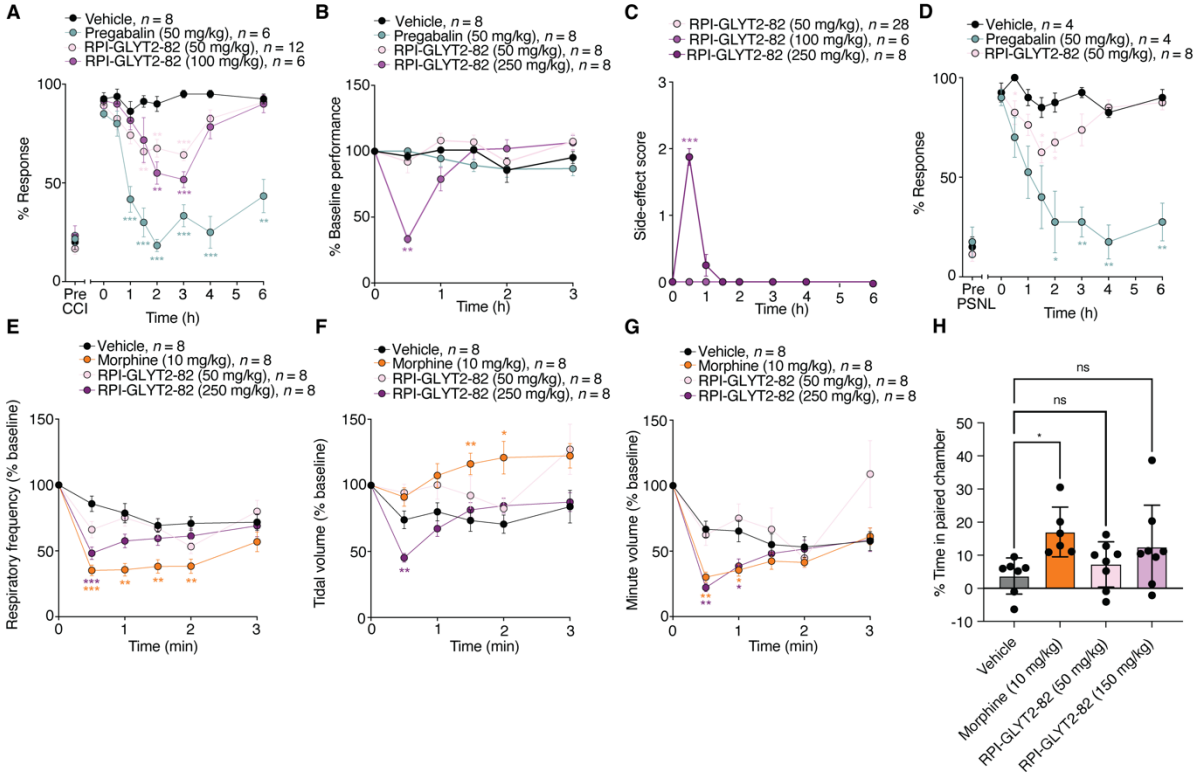

Figure 6. RPI-GLYT2-82 is anti-allodynic in mouse models of neuropathic pain. (A) RPI-GLYT2-82 reduced response rate to von Frey stimulus in CCI mice. Two-way ANOVA with Dunnett's multiple comparison post hoc test was conducted between mice administered vehicle and every other group. ANOVA showed significant main effects of time ($p<0.001$; $F(5, 149) = 27.3$) and treatment ($p<0.001$; $F(3, 28) = 48.3$), along with an interaction effect ($p<0.001$; $F(21, 196) = 6.30$). Both 50 and 100 mg/kg (i.p.) doses demonstrated efficacy in reducing mechanical allodynia, significant at 2- and 3-hours post-injection compared to vehicle ($p<0.01$ & $p<0.001$). The 50 mg/kg dose was also significant at 30 minutes ($p<0.01$). Both doses peaked at the 3-hour time point, with 30% and 42% reductions, respectively. (B) RPI-GLYT2-82 caused a transient reduction in rotarod performance at 250 mg/kg. (C) RPI-GLYT2-82 produced transient sedation at a maximal dose. (D) RPI-GLYT2-82 reduced response rate to von Frey stimulus in PSNL mice. Two-way ANOVA showed significant main effects of time ($p<0.001$; $F(4, 46) = 12.7$) and treatment ($p<0.001$; $F(2, 13) = 20.8$), along with an interaction effect ($p<0.001$; $F(14, 91) = 5.86$). A 50 mg/kg (i.p.) dose demonstrated efficacy in reducing mechanical allodynia, significant at 90 minutes and 2-hours post-injection compared to vehicle ($p<0.05$). This effect peaked at the 90-min time point, with 22.5% reductions. (E-F) RPI-GLYT2-82 (50 mg/kg and 250 mg/kg) was examined against positive control morphine (10 mg/kg) and vehicle (saline). Activity of compounds using whole-body plethysmography apparatus, measuring (E) respiratory frequency, (F) tidal volume, and (G) minute volume. Two-way ANOVA with Dunnett's multiple comparison post-hoc test was conducted between mice administered saline and every other group. (H) RPI-GLYT2-82 did not increase preference in a conditioned place preference paradigm. RPI-GLYT2-82 (50 and 150 mg/kg) was compared to positive control morphine (10 mg/kg) and vehicle (5% solutol, 95% PBS). One-way ANOVA with Dunnett's multiple comparison post-hoc test was conducted between mice administered vehicle and every other group. Data shown as mean ± SEM. Significance is denoted as: * = $p \leq 0.05$, ** = $p \leq 0.01$, and *** = $p \leq 0.001$. n = biological replicates.

Discussion

Recent insights into the pathophysiological adaptations underlying neuropathic pain have provided opportunities to discover new classes of pain-relieving compounds that address limitations of the existing treatments by targeting new mechanisms. The glycine transporter GlyT2 is a promising therapeutic target to modulate glycinergic signalling for the treatment of neuropathic pain; however, a structural understanding of transporter inhibition has proved

elusive. We have resolved the first structures of human GlyT2 bound to a potent pseudo-irreversible inhibitor, ORG25543, that failed in pre-clinical studies, and a novel and reversible inhibitor, RPI-GLYT2-82 as well as in a substrate-free state.

We show that RPI-GLYT2-82 is anti-allodynic in both the CCI and PSNL mouse models of neuropathic pain, shows no addiction liability at up to 3 times the minimal analgesic dose, and is devoid of mechanism-based side-effects. This is an essential milestone that has previously prevented many GlyT2 inhibitors from progressing past the pre-clinical stage.

We reveal that benzamide and related chemotype inhibitors bind from the extracellular side to an allosteric site, located in a crevice between TM1b and 10 and capped by the EL4, and lock the transporter in an outward-open state. The allosteric cavity collapses in the inward-open substrate-free state of GlyT2 with EL4 occupying the space (Figure 7). In the inward-open structure, the TM5 segment is unwound allowing solvation of the intracellular release pathway and the hinge-like motion of TM1a exposes the core of the transporter to the intracellular side (Figure 7). While we observe a loosely-bound Na^+ ion in the Na1 site only in the inhibitor-bound structures of GlyT2, the Cl^- ion remains bound in both outward- and inward-open conformational states of the transporter.

Intriguingly, ORG25543 and RPI-GLYT2-82 form similar interactions with GlyT2 suggesting that destabilising interactions are in part the drivers of reduced potency and increased reversibility of RPI-GLYT2-82. While the cryo-EM structures capture the stable binding modes of the inhibitors at cryo-temperatures, our MD simulations provide further insight into the dynamic nature of RPI-GLYT2-82 binding. Our simulations show a propensity for RPI-GLYT2-82 to partially enter the central substrate binding site, allowing the compound to adopt a more favourable geometry compared to the pose it adopts in the cryo-EM structure, and provides another dimension explaining the reversibility observed with RPI-GLYT2-82 binding. Exploiting this propensity provides an opportunity to limit the on-target side effects observed with pseudo-irreversible inhibitors.

The allosteric binding pocket on the extracellular side of the transporter is a particularly interesting pharmacological target as the sequence diversity of the site among the SLC6 transporters can be exploited to develop highly selective inhibitors for a variety of neurological disorders. We have previously shown that the conservative point mutation of L425I in EL4 of the closely related transporter, GlyT1, is sufficient to impart sensitivity of bioactive lipids, that are selective inhibitors of GlyT2[63]. This suggests that a similar allosteric binding site also exists in GlyT1. Our results will also allow further examination of the extent this allosteric site exists on the other closely related transporters, proline transporter (ProT, SLC6A7) and $ATB^{0,+}$ (SLC6A14), and the more distantly related neurotransmitter transporters of dopamine, serotonin and GABA. Recent studies on DAT bound to MRS7292[35] have also revealed an extracellular allosteric site that differs from the GlyT2 site we identified here, largely due to low sequence identity. Nonetheless, these two sites share notable structural features, pointing to a conserved mechanism that may inspire new approaches in drug discovery for the SLC6 family of transporters.

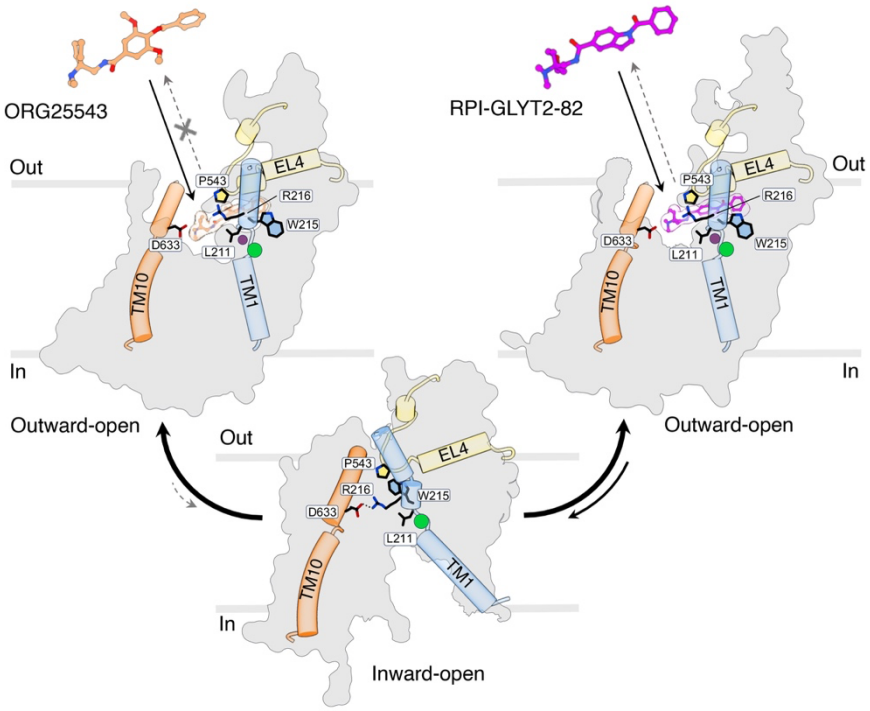

Figure 7. Allosteric inhibition of GlyT2. Schematic showing conformational differences between inhibitor-bound outward-open and substrate-free inward-open states of GlyT2. ORG25543 (orange) and RPI-GLYT2-82 (magenta) lock GlyT2 in an outward-open conformation. The key binding site residues stabilising the compounds, L211, W215, R216, P543 and D633, are shown as sticks. The slow off-rate of ORG25543 prohibits the transporter to cycle to an inward-open state, while RPI-GLYT2-82 binding to GlyT2 is reversible allowing the transporter to sample other conformational states after release. In the substrate-free inward-open state, the extracellular gate formed by R216 and D633 closes access to the extracellular side and W215 occupies the allosteric site. Chloride ion (green sphere) is bound in all states and sodium ion (purple sphere) in Na1 site is bound only in the inhibitor-bound states. Transmembrane helices TM1 and TM10 are shown in blue and orange, respectively, and EL4 is shown in yellow.

Limitations of the study

Whilst RPI-GLYT2-82 provides analgesia in mouse models of neuropathic pain without side effects or addiction liability, it is not as efficacious as the gold standard neuropathic pain drug, pregabalin. RPI-GLYT2-82, however, exhibits higher potency (IC_{50} = 0.55 μM, Figure 1C) for GlyT2 compared to opiranserin (IC_{50} = 0.86 μM)[62]. Furthermore, whilst GlyT2 is the primary target for RPI-GLYT2-82, it does show activity at 5HT2A receptor and the serotonin transporter. It is not clear as to how much of the analgesic effects are mediated by these other targets or whether the sedation observed at 5 times the minimal analgesic doses is a result of alternate target occupancy.

To overcome these limitations, the selectivity, occupancy and pharmacokinetics of allosteric GlyT2 inhibitors need to be optimized for analgesic efficacy. With insights gained from the reported cryo-EM structures here, structure-based drug design efforts will be reignited toward developing the next-generation of optimized RPI-GLYT2-82 analogues with improved *in vivo* analgesic efficacy. The structure activity- and structure-kinetic relationships data will be used to correlate GlyT2 inhibitor binding profiles, together with transporter occupancy percentages to analgesic efficacy and therapeutic index. We believe that the findings presented here provides additional data that highlight the potential promise that GlyT2 as the target holds for developing a safe and effective non-opioid analgesic for treating neuropathic pain. This study should spur further re-evaluation of GlyT2 as a target for chronic pain by the broader drug discovery community, potentially leading to the identification of novel GlyT2 inhibitors exhibiting a blend of optimal binding profiles, transporter occupancy, and pharmacokinetic characteristics. It lays the groundwork for the development of non-opioid pain therapeutics offering reduced addiction risks and greater efficacy against neuropathic pain.

ACKNOWLEDGEMENTS

We thank Shannon N. Mostyn for early contribution to producing the first GlyT2 constructs. We thank Julian P. Storm and other members of the ASH-lab for helpful discussions, and Dr. Roger Dawson for comments on the manuscript. The plasmid for expression of His-tagged HRV-3C protease was a kind gift from Dr. Eric R. Geertsma. This project has received funding from the Lundbeck Foundation (R368-2021-522) and the Novo Nordisk Foundation (NNF23OC0087107) to A.S., and the National Institute on Drug Abuse, USA, (NIH R01DA048879) to C.L.C. and R.J.V., and (NIDA IRP ZIA000069) to M.M. We thank L. Kristensen for access to the protein production facility at the Department of Drug Design and Pharmacology, University of Copenhagen. The cryo-EM data was collected at the Core Facility for Integrated Microscopy (CFIM), Faculty of Health and Medical Sciences, University of Copenhagen, supported by the Novo Nordisk Foundation (grants NNF17SA0024386 and NNF22OC0075808). We acknowledge the support offered at the CFIM by T. Pape and N. Sofos. Molecular dynamics simulations were supported by the Australian Government's National Collaborative Research Infrastructure Strategy (NCRIS), with access to computational resources provided by the National Computational Infrastructure and Pawsey Supercomputing Research Centre through the National Computational Merit Allocation Scheme.

AUTHOR CONTRIBUTIONS

C.L.C., R.J.V., and A.S. conceived and designed the project. C.L.C. and T.K.P. designed and synthesised RPI-GLYT2-82 compound. R.P.C.C. and A.S. established the protein expression and purification conditions. Expression, purification, cryo-EM sample preparations and data collections, processing, analysis and structure determination were carried out by R.P.C.C. with support from A.S. *In vitro* experiments were carried out by I.L. and R.P.C.C. with support from R.J.V. *In vivo* experiments were carried out by J.P-O, Z.J.F, and A.E.T with support from S.A.M., R.J.V., and M.M. The molecular dynamics studies were carried out by A.S.Q, and B.J.W-N, with support from M.L.O. R.P.C.C., R.J.V., and A.S. wrote the initial draft of the manuscript with contributions from all authors.

DECLARATION OF INTERESTS

C.L.C. and R.J.V. have a provisional patent application for compound RPI-GLYT2-82.

Supplemental information

The manuscript contains Data S1 and Data S2, Figures S1 – S7, Tables S1 – S4, and Methods S1.

RESOURCE AVAILABILITY

Lead contact

Further information and requests for resources and reagents will be directed and be fulfilled by Azadeh Shahsavar (ash@sund.ku.dk), the lead contact.

Materials availability

Unique reagents generated in this study are available from the Lead Contact on request.

Data and code availability

Atomic coordinates of GlyT2$^{\Delta 185}$ bound to ORG25543, RPI-GLYT2-82, or in substrate-free state have been deposited in the Protein Data Bank (PDB) under accession codes 9HUE, 9HUF, and 9HUG, respectively. The corresponding cryo-EM maps have been deposited in the Electron Microscopy Data Bank (EMDB) under accession numbers EMD-52409, EMD-52410, and EMD-52411, respectively. Molecular dynamics starting conformations, mdp files and

topologies are available at https://github.com/OMaraLab/GlyT2_2024. This paper does not report original code. Any additional information required to reanalyse the data reported in this paper is available from the lead contact upon request.

EXPERIMENTAL MODEL AND SUBJECT DETAILS

DH5α (New England Biolabs) and XL1-Blue Competent Cells (Agilent) were cultured in lysogeny broth (LB) at 37 °C to amplify plasmids.
Expi293F cells (ThermoFisher Scientific) were cultured in HE400AZ medium at 37 °C and 8% CO_2.
Xenopus laevis oocytes were stored at 18 °C in frog Ringer's solution (96 mM NaCl, 2 mM KCl, 1 mM $MgCl_2$, 1.8 mM $CaCl_2$, 5 mM HEPES, pH 7.5) supplemented with 2.5 mM sodium pyruvate, 0.5 mM theophylline, 50 µg/mL gentamicin and 100 µg/mL tetracycline.

Animals

The CCP behavioural experiments were performed with adult male C57BL/6J mice, 8-12 weeks old, obtained from The Jackson Laboratory (Maine, USA). Mice were housed in groups of four and had free access to food and water. Housing rooms were temperature and humidity controlled and maintained on a 12 h light/dark cycle. Experiments were conducted during the light phase.
All other behavioural experiments undertaken with male and female C57BL/6 mice, sourced from the Animal Research Centre (WA, Australia) or Australian BioResources (NSW, Australia). Mice were 6 weeks of age upon arrival and housed in individually ventilated cages (IVC, Sealsafe Plus Green Line, Techniplast) with Smart Flow Air Handling Units (Techniplast), lined with corncob bedding. Mice were housed in groups of 4 in a holding room maintained on a 12-hour light-dark cycle (0545 to 1745) maintained at 21 ± 2 ºC and relative humidity at 50 ± 5% with *ad libitum* access to food (Irradiated rat and mouse chow; Specialty Feeds, WA) and filtered water. Mice were given one week to habituate to the research facility and were then acclimatised to all aspects of the testing procedure including the observation room, handling by the experimenter, and the relevant testing apparatus. Animals were monitored at least twice a week for irregularities such as dehydration, skin conditions, and weight loss.
Pharmacokinetic studies were performed by Eurofins Discovery Partner with ICR mice. RPI-GLYT2-82 in-life plasma and BBB pharmacokinetic study was also conducted by Eurofins Discovery Partner with C57BL/6 mice. Male ICR mice weighing 30 ± 5 g and male C57BL/6 mice weighing 22 ± 2 g were provided by BioLasco Taiwan Co., Ltd. (under Charles River Laboratories Licensee). Animals were acclimated for 3 days prior to use and were confirmed to be in good health. The animals were housed in animal cages with a space allocation of 30 x 19 x 13 cm. All animals were maintained in a controlled temperature (20 - 24°C) and humidity (30% - 70%) environment with 12-h light/dark cycles. Free access to standard lab diet [MFG (Oriental Yeast Co., Ltd., Japan)] and autoclaved tap water were granted.

Ethics statement

Xenopus laevis oocytes were supplied by Victor Chang Cardiac Research Institute and approved by the Garvin Institute/St Vincents Hospital Animal Ethics Committee (Animal Research Authority 23_11). Non-CCP behavioural experiments were performed under approval from the Animal Ethics Committee of the University of Sydney (AEC protocol numbers 1363 and 2146). CCP behavioural experiments were conducted in accordance with the Guidelines of the Animal Care and Use Committee of the Intramural Research Program, National Institute on Drug Abuse, National Institutes of Health (ASP protocol 23-NRB-43). Pharmacokinetics studies conducted by Eurofins Discovery Partner including housing, experimentation, and animal disposal were performed in general accordance with the "Guide for the Care and Use of Laboratory Animals: Eighth Edition" (National Academies Press, Washington, D.C., 2011) in the AAALAC-accredited laboratory animal facility. In addition, the

animal care and use protocol was reviewed and approved by the IACUC at Pharmacology Discovery Services (PDS) Taiwan, Ltd.

GlyT2 construct

The human GlyT2 complementary DNA sequence was codon optimised and synthetised by Azenta for expression in mammalian cell. The GlyT2 construct contains a N-terminal deletion of residues 2 to 185 ($GlyT2^{\Delta 185}$). The sequence of $GlyT2^{\Delta 185}$ followed by a $G(GGGS)_3G$ linker, a HRV 3C protease cleavage site, enhanced green fluorescent protein (eGFP), a twin Strep-Tag II tag and a decahistidine tag were cloned into a pCDNA3.1 vector for transient transfection in Expi293F human cells (ThermoFisher Scientific). The Expi293F cell stock was authenticated by ThermoFisher Scientific. The cell line was regularly tested for mycoplasma contamination and tested negative for contamination. No misidentified cell lines were used.

METHOD DETAILS

Chemical Synthesis of RPI-GLYT2-82

All reactions were performed under a dry atmosphere of nitrogen unless otherwise specified. Indicated reaction temperatures refer to the reaction bath, while room temperature (rt) is noted as 25 °C. Commercial grade reagents and anhydrous solvents were used as received from vendors and no attempts were made to purify or dry these components further. Removal of solvents under reduced pressure was accomplished with a Buchi rotary evaporator at approximately 28 mm Hg pressure using a Teflon-linked KNF vacuum pump. The measurement of pH for neutralizations or acidifications was measured with Hydrion pH paper (MicroEssential Lab). Thin layer chromatography (TLC) was performed using 1” x 3” AnalTech No. 02521 silica gel plates with fluorescent indicator. Visualization of TLC plates was made by observation with either short wave UV light (254 nm lamp), 10% phosphomolybdic acid in ethanol, or in iodine vapours. Preparative thin layer chromatography was performed using Analtech, 20 × 20 cm, 1000-micron preparative TLC plates. Flash column chromatography was carried out using a Biotage Selekt Unit and a Biotage® Selekt System with Biotage Sfär silica gel columns. Proton NMR spectra were obtained on a 600 MHz Bruker AV III nuclear magnetic resonance spectrometer. Chemical shifts (δ) are reported in parts per million (ppm) and coupling constant (*J*) values are given in Hz, with the following spectral pattern designations: s, singlet; d, doublet; t, triplet, q, quartet; quint, quintet; m, multiplet; dd, doublet of doublets; dt, doublet of triplets; dq; doublet of quartets; br, broad signal. Tetramethylsilane was used as an internal reference. Peak listing, multiplicity designations, and coupling constant calculations were conducted using Mnova v.14 software (Mestrelab Research). Carbon NMR spectra were obtained on a 600 MHz Bruker AV III nuclear magnetic resonance spectrometer and tetramethylsilane was used as an internal reference. Any melting points provided are uncorrected and were obtained using a Stanford Research Systems OptiMelt melting point apparatus (MPA100) with an automated melting point system. Mass spectroscopic (MS) analyses were performed using ESI ionization on a Shimadzu LC-MS 2020 single quadrupole mass spectrometer with a binary solvent system A and B using a gradient elusion [A, H_2O with 0.01% trifluoroacetic acid; B, CH_3CN with 0.01% trifluoroacetic acid] and flow rate = 0.5 mL/min). A Shimadzu Nexcol C18 5µM, 50 x 3.0 mm was used. High pressure liquid chromatography (HPLC) purity analysis was performed using a Shimadzu LC-2050C with a binary solvent system A and B using a gradient elusion [A, H_2O with 0.01% trifluoroacetic acid; B, CH_3CN with 0.01% trifluoroacetic acid] and flow rate = 0.5 mL/min, with UV detection at 254 nm (system equipped with a photodiode array (PDA) detector). An X Bridge C18 5µm 4.6 x 150 mm was used. High resolution mass spectrometry (HRMS) analysis was performed using a Thermo Scientific Orbitrap Eclipse Tribrid mass spectrometer. Structural confirmation of RPI-GLYT2-82 was determined via ^1H NMR, ^{13}C NMR, and HRMS and the purity was assessed to be ≥95% via ^1H NMR, ^{13}C NMR, and HPLC. The detailed procedures are shown in Methods S1.

Expression of GlyT2

GlyT2$^{\Delta 185}$ was expressed in HE400AZ expression medium (GMEP Cell Technologies, Japan) in 600 mL TubeSpin bioreactors, incubating in an orbital shaker at 37 °C, 8% CO_2 and 175 rpm in a humidified atmosphere. The Expi293F cells (ThermoFisher Scientific; authenticated and free of mycoplasma contamination) were transfected at a density of 3.0 – 3.5 × 10^6 cells per mL and a viability of above 97%. A 25 kDa linear polyethylenimine (LPEI) was used as the transfection reagent, at a GlyT2 DNA:LPEI ratio of 1:2 with a total plasmid concentration of 2.0 μg per mL of culture volume to transfect. The LPEI/DNA complexes were incubated in Opti-MEM™ I Reduced Serum Medium (ThermoFisher Scientific) for 15 minutes before adding to the cells. At approximately 17 hours post-transfection, cell cultures were supplemented with 10 mM sodium butyrate. The cells were harvested at approximately 44 h post-transfection at a viability of above 70% and stored at -70 °C until purification.

Purification of GlyT2

The cell pellets were thawed on ice and resuspended in 50 mM Tris-HCl (pH 7.5), 150 mM NaCl, 20% glycerol (v/v), 1 cOmplete™ Protease Inhibitor Cocktail tablet per 50 mL of buffer (Roche), 0.25 mg of DNAse I and incubated on rotation for 30 minutes at 4 °C. The suspension was solubilised in 1% (w/v) n-dodecyl-β-D-maltopyranoside (DDM) supplemented with 0.1% cholesterol hemisuccinate (CHS) with 15-25 μM brain polar lipids extract (Avanti) for 45 minutes at 4 °C. Cell debris was removed by centrifugation at 140, 000 g, 4 °C for 20 minutes. To the cleared lysate, StrepTactin XT Sepharose chromatography resin (Cytiva) was added in batch and incubated overnight at 4 °C, with stirring.
The resin was washed with 10 column volumes (CV) of buffer containing 50 mM Tris-HCl (pH 7.5), 150 mM NaCl, 0.1% (w/v) GDN, 0.1% (w/v) LMNG, 0.02% (w/v) CHS and 15-25 μM brain polar lipids extract. The resin was subsequently washed with 20 CV of the same buffer supplemented with 10 mM MgCl2 and 2 mM adenosine 5′-triphosphate disodium salt hydrate (ATP). The resin was then washed with 10 CV of buffer containing 50 mM Tris-HCl (pH 7.5), 150 mM NaCl, 0.05% (w/v) GDN, 0.05% (w/v) LMNG, 0.01% CHS, and 15-25 μM brain polar lipids extract. The protein was eluted in the same buffer supplemented with 20% glycerol (v/v) and 50 mM biotin (pH 8). The protein was then treated with HRV-3C protease (in-house) for 3 hours at 10 °C to cleave the eGFP–twin-Strep-Tag-His tag, while being dialysed in buffer containing 50 mM Tris-HCl (pH 7.5), 150 mM NaCl, 0.003% (w/v) GDN, 0.003% (w/v) LMNG, 0.0006% (w/v) CHS and 20% glycerol (v/v). The eGFP–twin-Strep-Tag-His tag was removed by passing the sample through a nickel-nitrilotriacetic acid (Ni-NTA) HisTrap™ HP column (Cytiva) and impurities were removed by anion exchange chromatography with a pre-packed 1 mL HiTrap™ Q HP column (Cytiva). The sample was concentrated to above 2 mg per mL, using an Amicon Ultra-15 centrifugal filter unit (Merck) with a 100,000 dalton cut-off, flash frozen in liquid nitrogen and stored at -80 °C.
On the day of grid preparation, the sample was further purified and buffer exchanged by size exclusion chromatography in buffer containing 50 mM Tris-HCl (pH 7.5), 150 mM NaCl, 0.008% (w/v) GDN, 0.008% (w/v) LMNG, 0.0016% (w/v) CHS using a Shodex kW803 column connected to an Äkta Go purifier system. Fractions were concentrated to above 4 mg per mL and ultracentrifuged at 100,000 g for 30 minutes.
For purification of the ORG25543-bound GlyT2$^{\Delta 185}$ sample, cell pellets were resuspended in the buffer supplemented with 100 μM ORG25543 (Tocris), and 10 μM ORG25543 was maintained in all the buffers throughout the purification. For the substrate-free GlyT2$^{\Delta 185}$ sample, resuspension buffer was supplemented with 100 μM ODLys and subsequent buffers were supplemented with 10 μM ODLys throughout the purification. For the RPI-GLYT2-82-bound GlyT2$^{\Delta 185}$ sample, the protein was purified without inhibitor and was incubated with 100 μM RPI-GLYT2-82 for 45 minutes on ice prior to SEC on the day of grid preparation. The SEC buffer was supplemented with 100 μM RPI-GLYT2-82.

Cryo-EM grid preparation and data collection

Immediately prior to grid preparation, the protein sample was supplemented with 0.01% (w/v) of fluorinated octyl maltoside (Anatrace). UltrAuFoil grids (R1.2/1.3 300 mesh, Quantifoil) were glow discharged (Leica EM ACE200) at 15 mA for 90 s. 3 μL of sample was applied to the

grids, blotted for 5 s with a blot force of -3 before being plunge-frozen in liquid ethane using a Vitrobot mark IV (ThermoFisher) at 100% humidity and 4 °C in an environmental chamber. Movies were collected in counting mode at 165,000× magnification (300 kV), yielding a raw pixel size of 0.728 Å per pixel, using EPU 3.6 software (ThermoFisher) on a Titan Krios G2 (ThermoFisher) equipped with a Selectris X energy filter set to a slit width of 10 eV and a Falcon 4i direct electron detector (ThermoFisher). A defocus value range of –0.6 to –1.8 µm and a dose rate of around 10.2 electrons (e) per pixel per second were used, giving a total dose of 60 e/Å^2 per movie (see Data S1).

Cryo-EM data processing

The cryo-EM data sets were processed using cryoSPARC v.4.5.3[65]. A total of 12,374 movies were collected for the ORG25543-bound GlyT2$^{\Delta185}$ sample, 16,094 for the RPI-GLYT2-82-bound GlyT2$^{\Delta185}$ sample, and 21,335 for the substrate-free GlyT2$^{\Delta185}$ sample. The movies were motion corrected using Patch Motion Correction with default parameters. The contrast transfer function (CTF) parameters were estimated using Patch CTF Estimation and exposures with a CTF fit resolution of less than 3.6 Å were excluded during curation, yielding 11,378 exposures for ORG25543-bound GlyT2$^{\Delta185}$, 14,629 for RPI-GLYT2-82-bound GlyT2$^{\Delta185}$, and 20,392 for the substrate-free state.

For the ORG25543-bound GlyT2$^{\Delta185}$ sample, particles were picked by reference-free blob picker using a minimum and maximum particle diameter of 90 Å and 160 Å, respectively. A total of 2,807,000 particles were picked initially. Particles were then extracted with a box size of 300 pixels, Fourier cropped to 256 pixels and used to generate templates following a 2D classification, ab initio, heterogeneous refinement and non-uniform refinement[83]. Particles were then picked with the newly generated templates and extracted with a box size of 300 pixels (Data S1). Following a 2D classification, a multi class ab initio and subsequent heterogeneous refinement were performed. A further heterogeneous refinement was performed using the selected particles. Suboptimal particles were removed by 3D classification and 2D classification. Selected particles were used for a one-class ab initio followed by a non-uniform refinement with initial low-pass resolution of 12 Å, deactivated dynamic mask start resolution and with the minimize over per-particle scale parameter on. Per-particle movement trajectories and empirical dose weights were estimated using reference-based motion correction followed by a final non-uniform refinement resulting in a 3D reconstruction of ORG25543-bound GlyT2$^{\Delta185}$ map at 2.49 Å resolution, based on a Fourier shell correlation (FSC) cutoff of 0.143 with 283,838 particles.

For the RPI-GLYT2-82-bound GlyT2$^{\Delta185}$ and substrate-free GlyT2$^{\Delta185}$ sample, templates were generated from the ORG25543-bound GlyT2$^{\Delta185}$ final map and used to pick particles. Subsequent data processing was similar to the ORG25543-bound GlyT2$^{\Delta185}$ data processing pipeline (Data S1). Final non-uniform refinement for RPI-GLYT2-82-bound GlyT2$^{\Delta185}$ and substrate-free GlyT2$^{\Delta185}$ resulted in 3D reconstruction maps at 2.79 Å and 2.97 Å resolution with 201,519, and 180,698 particles, respectively.

Model building and refinement

The initial GlyT2$^{\Delta185}$ structure model was derived using AlphaFold2 (AF-Q9Y345-F1)[84]. The predicted model was manually fitted into the cryo-EM map in UCSF ChimeraX[68] v1.8 and was initially refined using Namdinator[70]. The models were refined using Phenix[67] v1.21.1-5286 followed by visual examination and manual rebuilding in Coot[66] v0.9.8.6 and ISOLDE[69] v1.6. The ligand-restraint files for refinement were generated by phenix.elbow. Figures were prepared using ChimeraX[68] v1.8.

The final models of ORG25543-bound GlyT2$^{\Delta185}$ and RPI-GLYT2-82-bound GlyT2$^{\Delta185}$ lack the initial methionine residue, residues 335–364 in EL2, and the last 13 residues of the C terminus. The final model of substrate-free GlyT2$^{\Delta185}$ lacks residues 185–194 from the N terminus, residues 330–364 in EL2, and the last 12 residues of the C terminus. Refinement and validation statistics are presented in Data S1.

Expression and functional analysis of GlyT2^{WT}, GlyT2$^{\Delta185}$, and mutant GlyT2 in *Xenopus laevis* oocytes

Stock solutions of 50 mM ORG25543, and 20 mM RPI-GLYT2-82 were dissolved in dimethyl sulfoxide (DMSO) and diluted in frog Ringer's solution (96 mM NaCl, 2 mM KCl, 1 mM $MgCl_2$, 1.8 mM $CaCl_2$, 5 mM HEPES, pH 7.5) to desired concentrations. Final solutions contained less than 0.001% DMSO, a concentration that had no effect on transporter function.
Human GlyT2a wild type (herein referred to as GlyT2) and codon optimised $GlyT2^{\Delta185}$ complementary DNA were subcloned into the plasmid oocyte transcription vector (pOTV). Site-directed mutagenesis was performed using traditional PCR techniques and sequenced by the Australian Genome Research Facility (Sydney, Australia). Purified plasmid DNAs were linearised with SpeI (New England Biolabs, Catalogue number R3133S). Complementary RNA was transcribed by the T7 RNA polymerase using the mMESAGE mMACHINE T7 kit (Ambion, Cat# AM1344).
Stage V *Xenopus laevis* oocytes were detached from the lobe by digestion with 2 mg/mL collagenase A (Boehringer, Mannheim, Germany). Defolliculated stage V oocytes were injected with 20 ng of cRNA encoding $GlyT2^{WT}$, $GlyT2^{\Delta185}$, or mutant GlyT2 (Drummond Nanoinject, Drummond Scientific Co., Broomall, PA, USA). The oocytes were stored at 18°C in frog Ringer's solution, which was supplemented with 2.5 mM sodium pyruvate, 0.5 mM theophylline, 50 µg/mL gentamicin and 100 µg/mL tetracycline for 3-6 days, until transporter expression was adequate for measurement using the two-electrode voltage clamp technique. Whole-cell glycine transport currents were recorded at -60 mV using a Geneclamp 500 amplifier (Axon Instruments, Foster City, CA, USA) with a Powerlab 2/20 chart recorder (ADInstruments, Sydney, Australia). LabChart version 8 software (ADInstruments, Sydney, Australia) was used to process and visualise current traces.
Glycine concentration (1–300 µM) dependent transport currents were measured for $GlyT2^{WT}$ and $GlyT2^{\Delta185}$ ($n = 5$). Cumulative inhibitor concentration-dependent transport current responses were measured for ORG25543 (0.3–300 nM) and RPI-GLYT2-82 (0.01–10 µM). The substrate EC_{50} for $GlyT2^{WT}$, $GlyT2^{\Delta185}$, or mutant GlyT2 was applied and then increasing concentrations of inhibitor were co-applied. Competition assays were performed using the same method as used for the glycine concentration dependent transport currents, with the co-application of RPI-GLYT2-82 at concentrations < 3-fold IC_{50}, IC_{50}, and > 3-fold IC_{50}. The concentration responses curves were analysed by Eadie-Hofstee plots to determine the mode of competition. Reversibility was determined by using the previously determined IC_{50} of ORG25543 or RPI-GLYT2-82. The glycine EC_{50} for $GlyT2^{WT}$, $GlyT2^{\Delta185}$, or mutant GlyT2 was applied and then the IC_{50} of the inhibitor was co-applied until the current plateaued. The cell was then continuously perfused with frog Ringer's solution to wash out the inhibitor from the bath solution. Every 5 min, glycine (EC_{50}) was re-applied for 1 min, and repeated for a total wash period of 30 min or until complete transporter recovery.

Electrophysiology data analysis

Data was analysed using GraphPad Prism 10 (version 4.0, GraphPad Software, San Diego, USA). Currents for each cell were normalised to the current generated by a maximal substrate concentration to account for the difference in transporter expression between cells. *n* refers to biological samples and not technical replicates.
The EC_{50} for glycine transport by GlyT2 was determined using the equation below:

$$I/I_{max} = [Gly]/(EC_{50} + [Gly])$$

Where I is the change in current from baseline (nA), and I_{max} is the current generated by a maximal glycine concentration as determined by Michaelis-Menten kinetics.
Competition assays were determined using the same method as the glycine dose responses, with I_{max} set to the maximal response from glycine (300 µM) in the absence of inhibitor (I_{300}). Data from the glycine dose responses were transformed using the Eadie-Hofstee function to confirm the mechanism of inhibition for each hit compound. The Y-axis remains the same, and transformation of the x-axis is as follows:

$$[Gly] \text{ transformed by } I/I_{300}/[Gly]$$

The IC_{50} values for inhibitors were determined using the equation below:

$$I/I_{EC50} = Bottom + (Top- Bottom)/(1+10^{(x-logIC50)})$$

Where I is current (nA), and I_{EC50} is the current generated by the EC_{50} (μM) glycine concentration in the absence of inhibitor. Top and Bottom are the maximal and minimal (≥ 0) plateau responses respectively, x is the concentration of inhibitor (nM), and IC_{50} is the concentration that causes 50% maximal inhibition.
Washout kinetics were fitted using the equation below:

$$\text{Recovery} = (Y_0 - \text{Plateau}) \times e^{-Kt} + \text{Plateau}$$

Where recovery is the amount of transport-dependent current restored as a percentage of pre inhibitor levels (%), Y_0 is the point which crosses the Y axis (≥ 0) and increases to the Plateau (≤ 100) in one phase, K is the rate constant (1/time), and t is time (mins).

In vivo characterisation

Drug preparation

Pregabalin (50 mg/kg) and RPI-GLYT2-82 were dissolved in a vehicle of 5% Solutol in PBS. For PSNL experiments, a vehicle of 10% Solutol and 1% DMSO in 0.9% saline was used. All solutions were prepared on the morning of experimentation in 3-5 mL glass v-vials immediately following baseline behavioural measurements. Mice were randomly assigned to a drug group by a second researcher using randomisation software (random.org), and the experimenter was blind to group allocations until after data collection. Compounds were administered via a single 200 μL i.p. injection into the lower right quadrant of the abdomen using 29-G insulin needles.

Chronic constriction injury and peripheral sciatic nerve ligation models of neuropathic pain

Neuropathic pain models were established via nerve injury to the left sciatic nerve via chronic constriction injury (CCI)[85] via 2 mm polyethylene cuff or partial sciatic nerve ligation (PSNL) via silk suture tightly constricting 1/3 – 1/2 of the nerve proximal to the trifurcation[86]. Mice were allowed to recover for 14 days after surgery prior to behavioural testing.

Mechanical allodynia assessment

Changes in sensitivity to a non-noxious mechanical stimulus was assessed by using a modified von Frey test. A single calibre of nylon filament that elicited approximately 15% response rate in naïve animals (0.4 g force) was applied to the plantar surface of the left hind paw until it just bent. Responses were defined as brisk withdrawal, shaking, or licking of the hind paw. Mechanical allodynia was assessed prior to surgery (baseline) and on the day of testing prior to drug administration (t = 0) and at 0.5, 1, 1.5, 2, 3, 4, and 6 hours post injection. Exclusion criteria were response rates > 30% at baseline or < 70% on the test day at t = 0. Data are presented as the percentage of responses out of 10 applications of the filament.

Rotarod

Motor coordination was assessed in naïve mice using an accelerating Rotarod, using large cylinders (69.5-mm diameter, 99-mm width, 27-cm drop to landing platform) with speed increasing from 4 rpm to 20 rpm over 180 seconds. Mice underwent 3 days of training with 3 training sessions per day at 30-minute intervals. Mice were allowed 5 min of acclimatisation on cylinders at the start of each training day. On test day, mice were tested at t = 0 and then 30, 60, 90, 120, and 180 minutes after drug administration. Data were normalised to % baseline.

Side effect scoring

Throughout any given behavioural assessment, all animals were also monitored for adverse clinical events using a numerical rating scale (Table S4). The measures assessed included hypoxia, sedation, inactivity, piloerection or shivering, pain/discomfort, dehydration, weak tone, and convulsions. Adverse events were recorded at each time point, observed when placed in the testing apparatus, and scored on a scale of 0 – 3 where 0 = none, 1 = mild, 2 = moderate, and 3 = severe. Scores were averaged for each treatment group.

Respiratory depression assessment

Respiratory function was assessed in naïve, uninjured mice via a whole-body plethysmography apparatus consisting of two parallel chambers connected to a pressure transducer (Buxco, DSI Instruments, USA). Mice were acclimatised to the chambers for 15 minutes on the two days preceding the experiment. Chambers were covered with a lab coat and divided with an opaque barrier to prevent any unwanted visual stimulation. On the day of experimentation, mice were acclimatised for 20 minutes, the last 5 of which were taken as the baseline. Mice were briefly removed from the chamber for injection, before being returned to the chamber. Respiratory function was then measured for a period of 5 minutes at 30, 60, 90, 120, and 180 minutes post-injection. Respiratory frequency, tidal volume (TVb) and minute volume (MVb) were recorded on the accompanying computer software (Buxco, FinePointe, DSI Instruments). All data were averaged and normalised to percentage (%) of baseline and analysed via two-way ANOVA with Dunnett's post hoc multiple comparisons (GraphPad Prism v10, GraphPad software, USA).

Conditioned Place Preference (CPP)

The CPP apparatus (Stoelting Co.) consisted of one middle (10 cm x 20 cm) and two outer chambers (18 cm x 20 cm). The middle chamber had bare walls with a smooth floor. One outer chamber had stripes on the walls with a smooth floor and the other had circles on the walls with a textured floor. CPP consisted of three stages: pretesting, conditioning, and testing. Pretesting occurred on the first two days. Mice were placed in the middle chamber and allowed to freely explore the entire apparatus for 20 minutes. Time spent in each chamber was recorded using ANY-maze software (Stoelting Co.) and averaged across the two pretest days to determine baseline preferences. For the next eight days mice received intraperitoneal injection of test drugs (morphine, RPI-GLYT2-82) or vehicle on alternate days. Conditioning sessions lasted 40 minutes during which mice only had access to one of the outer chambers. Drugs were administered in the animals least preferred chamber identified during pretesting as this biased approach has been shown to produce reliable CPP with morphine in mice[87]. The CPP test was performed on day eleven using the same conditions as pretesting. Preference score was calculated as the percent change in time spent in the drug-paired chamber on the test day compared to pretesting. A ROUT test (Q = 10%) was used to remove outliers before performing an ordinary one-way ANOVA with Dunnett's multiple comparisons test to analyse differences between vehicle and drug treated groups.

Molecular dynamics simulations

Molecular dynamics simulations of membrane-embedded GlyT2–ORGH were initiated from the GlyT2 structures with bound inhibitors using the GROMACS 2023 MD package in conjunction with the GROMOS 54a7 forcefield[71]. The GROMOS 54a7 force field was chosen as it has been specifically parameterised to reproduce the experimental solvation free enthalpy and partition coefficients between polar and nonpolar environments for a range of chemical compounds and is ideally suited for lipid and membrane protein simulations. As the cryo-EM model contained a discontinuity between 330 and 364, acetyl and NH_2 caps were applied to avoid the introduction of inappropriate charges. The disulfide bond (C311 and C320 (EL2)) was explicitly included. The protonation state of the side chains of ionizable residue was assigned according to the pKa predicted using PROpKa[75,76] version 3.5.1.
Parameters for cholesterol hemisuccinate, ORG255432 and RPI-GLYT2-82 were generated using the Automated Topology Builder 3.069 (CHS molid 1736730[88], ORG25543 molid 727769[89], RPI-GLYT2-82 molid 1732579[90])[77]. The pKa of the ORG25543 and RPI-GLYT2-82 amide groups were estimated with molgpka[78] (ORG25543 pKa 8.4, RPI-GLYT2-82 pKa 8.4), and the compounds were simulated with the pendant ammonium protonated[78].
Proper dihedrals of benzamide groups were refined using a using a tool that will be included in the next release of the ATB[77] (ORG25543 R_1–R_3 benzamide k_Φ = 18.31 kJ/mol/deg, RPI-GlyT2-82 R_1–R_2 benzamide k_Φ = 22.28 kJ/mol/deg, RPI-GlyT2-82 R_1–R_3 benzamide = 21.75 kJ/mol/deg). Benzamide dihedrals were fitted to the difference between

the energy obtained by DFT (wB97X/6-31Gd) and energy minimisation with the ATB force field for dihedral angles constrained to 25 values between -180 and 180 degrees.
Two simulation systems were prepared, one using the GlyT2/ORG25543 cryo-EM complex, and a second using the GlyT2/RPI-GLYT2-82 complex. The cryo-EM structures of each GlyT2 complex, containing ligand, bound chloride and bound sterols, was embedded in an 80% POPC and 20% cholesterol lipid bilayer created using the MemGen webserver[79]. Each system was solvated with simple point charge (SPC) water, chosen for compatibility with the GROMOS 54a7 forcefield, and 150 mM NaCl for physiological relevance[91]. Counterions were added to ensure overall charge neutrality. All simulations were carried out under periodic boundary conditions. Systems were energy minimized using the steepest descent algorithm then equilibrated with decreasing harmonic restraints on the protein, bound ligand, and bound sterols in five sequential 2 ns simulations with a 2 fs timestep (1000 kJ/mol/nm^2, 500 kJ/mol/nm^2, 100 kJ/mol/nm^2, 50 kJ/mol/nm^2, 10 kJ/mol/nm^2). Solute hydrogen masses were repartitioned to access longer simulation timesteps[92] then the repartitioned systems were equilibrated with an additional 2 ns simulation using a 4 fs timestep, with 10 kJ mol^{-1} nm^{-2} harmonic restraints on the protein, ligand, and bound sterols.
The coordinates from the final frame of each equilibrated system were used as the starting configuration for 500 ns production simulations, using a 4 fs timestep. To increase the statistical sampling of the GlyT2/ligand conformation space and ensure convergence of the docked compounds, non-biased production simulations of each system were performed multiple replicate simulations (GlyT2/ORG25543 n=6, GlyT2/RPI-GLYT2-82 n=3). Random starting velocities were assigned at the start of each replicate simulation according to a Boltzmann distribution. The temperature was maintained at 310 K using the Bussi-Donadio-Parrinello velocity rescale thermostat and a coupling constant of 0.1 ps[93]. The pressure was maintained at 1 bar using semi-isotropic pressure coupling with the Parrinello--Rahman barostat[94] using a 5 ps coupling constant and an isothermal compressibility of 4.5×10^{-5} bar $^{-1}$. SETTLE[95] was used to constrain the geometry of water molecules and LINCS[96] was used to constrain the covalent bond lengths of the solute. The electrostatic interactions were calculated using the Particle Mesh Ewald summation, and non-covalent interactions were determined via the Verlet scheme with a 1.4 nm cut-off.
Simulations were visualized using VMD v1.9.4a5575[74]. R.m.s.d. and r.m.s.f. analysis was performed on frames collected at 1 ns intervals, using gromacs tools. Energy landscapes were calculated on frames collected at 0.1 ns intervals with PLUMED version 2.9[72,73]. Per residue contacts and hydrogen bonding frequency analyses were performed on frames collected at 1 ns with VMD v1.9.4a5575[74]. Sodium density was performed on frames collected at 1 ns with MDAnalysis version 2.7.0[82]. Molecular Mechanics-Poisson Boltzmann/Surface Area (MM-PB/SA) was used for binding enthalpy decomposition[46,48]. Per ligand enthalpic contributions to binding were calculated with g_mmpbsa[80] on the first 50 ns of each replicate simulation, with frames spaced by 1 ns.

Analysis of MM-PBSA binding enthalpy

MM-PBSA[46,48] calculations were performed using the one-trajectory method[46,48,97] on the first 50 ns of MD simulation time for GlyT2/ORG5543 and GlyT2/RPI-GLYT2-82 systems, where the ligand remained in its experimentally determined pose. Binding entropy changes were not calculated. Frames were extracted at 1 ns intervals, yielding 50 frames per simulation for analysis.
The *g_mmpbsa*[98] module of GROMACS was used to compute binding enthalpies with a grid spacing of 0.5 Å, a solvent probe radius of 1.4 Å, γ = 0.03 kJ/mol/Å^2, and an external solute (saline) dielectric constant of 80. To address variations in internal solute dielectric across the full protein, the analysis was restricted to the ligand (experimental pose) and its binding site residues: 211, 212, 213, 215, 216, 286, 287, 290, 433, 520, 541, 542, 543, 545, 546, 547, 550, 567, 570, 571, 574, 629, and 633. Focusing on the binding site enabled MM-PBSA calculations using a consistent internal solute dielectric value, eliminating contributions from distal residues to the binding site with a different solute dielectric value.

Electrostatic analysis using the APBS webserver[99] revealed binding site surface electric potentials ranging from approximately -15 to -30 kT/e for most of the binding site. This variation in surface electric potential afforded a solute dielectric range of 10-20 across the GlyT2 binding site. The conversion from surface electric potential to solute dielectric was done using Equation **1**[100,101]. Here, ϕ is the surface electrostatic potential (in units of kT/e) from the APBS webserver[99], q is the charge of an electron, ξ_0 is the vacuum permittivity constant, ξ_s is the internal solute dielectric for MM-PBSA, and r is set to the interaction cut-off distance from the MD simulations (r = 1 nm). Specifically, ξ_0 is scaled by ξ_s, such that $\xi_0\xi_s$ accounts for the overall permittivity of the medium. Equation **1** is reduced to the relationship from Coulomb's law when ξ_s = 1.

$$|\phi| = \frac{|q|}{4\pi\, \xi_0\, \xi_s\, r} \qquad \textbf{(1)}$$

We chose ξ_s= 10 for two reasons: A) Equation **1** afforded values of ξ_{solute} between ~10-20; and, B) for $\xi_s$values between 10-20, the resultant MM-PBSA calculation with ξ_{solute}= 10 yielded a ratio of RPI-GLYT2-82/ORG25543 binding enthalpy (0.83-0.92, 95% C.I.) that was the most consistent with the experimental log(IC_{50}) ratio of RPI-GLYT2-82/ORG25543 (0.79). Specifically, ξ_{solute}= 10 gave the best qualitative agreement with experiment. Binding enthalpies and per-residue enthalpy contributions were reported as mean values ± the 95% confidence interval in energy (Figure S6). We did not report per-residue binding energy benefits/penalties > 2 kT (5.15 kJ/mol).

References

1. Finnerup, N.B., Attal, N., Haroutounian, S., McNicol, E., Baron, R., Dworkin, R.H., Gilron, I., Haanpaa, M., Hansson, P., Jensen, T.S., et al. (2015). Pharmacotherapy for neuropathic pain in adults: a systematic review and meta-analysis. Lancet Neurol *14*, 162-173. 10.1016/S1474-4422(14)70251-0.
2. Colloca, L., Ludman, T., Bouhassira, D., Baron, R., Dickenson, A.H., Yarnitsky, D., Freeman, R., Truini, A., Attal, N., Finnerup, N.B., et al. (2017). Neuropathic pain. Nat Rev Dis Primers *3*, 17002. 10.1038/nrdp.2017.2.
3. Lu, Y., Dong, H., Gao, Y., Gong, Y., Ren, Y., Gu, N., Zhou, S., Xia, N., Sun, Y.Y., Ji, R.R., and Xiong, L. (2013). A feed-forward spinal cord glycinergic neural circuit gates mechanical allodynia. J Clin Invest *123*, 4050-4062. 10.1172/JCI70026.
4. Aroeira, R.I., Sebastiao, A.M., and Valente, C.A. (2014). GlyT1 and GlyT2 in brain astrocytes: expression, distribution and function. Brain Struct Funct *219*, 817-830. 10.1007/s00429-013-0537-3.
5. Vandenberg, R.J., Ryan, R.M., Carland, J.E., Imlach, W.L., and Christie, M.J. (2014). Glycine transport inhibitors for the treatment of pain. Trends in Pharmacological Sciences *35*, 423-430. https://doi.org/10.1016/j.tips.2014.05.006.
6. Cioffi, C.L. (2018). Modulation of Glycine-Mediated Spinal Neurotransmission for the Treatment of Chronic Pain. J Med Chem *61*, 2652-2679. 10.1021/acs.jmedchem.7b00956.
7. Harvey, R.J., and Yee, B.K. (2013). Glycine transporters as novel therapeutic targets in schizophrenia, alcohol dependence and pain. Nat Rev Drug Discov *12*, 866-885. 10.1038/nrd3893.
8. Aubrey, K.R., Rossi, F.M., Ruivo, R., Alboni, S., Bellenchi, G.C., Le Goff, A., Gasnier, B., and Supplisson, S. (2007). The transporters GlyT2 and VIAAT cooperate to determine the vesicular glycinergic phenotype. J Neurosci *27*, 6273-6281. 10.1523/JNEUROSCI.1024-07.2007.
9. Rousseau, F., Aubrey, K.R., and Supplisson, S. (2008). The glycine transporter GlyT2 controls the dynamics of synaptic vesicle refilling in inhibitory spinal cord neurons. J Neurosci *28*, 9755-9768. 10.1523/JNEUROSCI.0509-08.2008.
10. Wilson, B.S., Peiser-Oliver, J., Gillis, A., Evans, S., Alamein, C., Mostyn, S.N., Shimmon, S., Rawling, T., Christie, M.J., Vandenberg, R.J., and Mohammadi, S.A. (2022). Peripheral Administration of Selective Glycine Transporter-2 Inhibitor, Oleoyl-$_D$-Lysine, Reverses Chronic Neuropathic Pain but Not Acute or Inflammatory Pain in Male Mice. Journal of Pharmacology and Experimental Therapeutics *382*, 246. 10.1124/jpet.122.001265.
11. Mostyn, S.N., Rawling, T., Mohammadi, S., Shimmon, S., Frangos, Z.J., Sarker, S., Yousuf, A., Vetter, I., Ryan, R.M., Christie, M.J., and Vandenberg, R.J. (2019). Development of an N-Acyl Amino Acid That Selectively Inhibits the Glycine Transporter 2 To Produce Analgesia in a Rat Model of Chronic Pain. J Med Chem *62*, 2466-2484. 10.1021/acs.jmedchem.8b01775.
12. Morita, K., Motoyama, N., Kitayama, T., Morioka, N., Kifune, K., and Dohi, T. (2008). Spinal antiallodynia action of glycine transporter inhibitors in neuropathic pain models in mice. J Pharmacol Exp Ther *326*, 633-645. 10.1124/jpet.108.136267.
13. Motoyama, N., Morita, K., Shiraishi, S., Kitayama, T., Kanematsu, T., Uezono, Y., and Dohi, T. (2014). Relief of cancer pain by glycine transporter inhibitors. Anesth Analg *119*, 988-995. 10.1213/ANE.0000000000000388.
14. Mingorance-Le Meur, A., Ghisdal, P., Mullier, B., De Ron, P., Downey, P., Van Der Perren, C., Declercq, V., Cornelis, S., Famelart, M., Van Asperen, J., et al. (2013). Reversible inhibition of the glycine transporter GlyT2 circumvents acute toxicity while preserving efficacy in the treatment of pain. Br J Pharmacol *170*, 1053-1063. 10.1111/bph.12343.

15. Yoshikawa, S., Oguchi, T., Funahashi, Y., de Groat, W.C., and Yoshimura, N. (2012). Glycine transporter type 2 (GlyT2) inhibitor ameliorates bladder overactivity and nociceptive behavior in rats. Eur Urol *62*, 704-712. 10.1016/j.eururo.2012.01.044.
16. Benito-Munoz, C., Perona, A., Felipe, R., Perez-Siles, G., Nunez, E., Aragon, C., and Lopez-Corcuera, B. (2021). Structural Determinants of the Neuronal Glycine Transporter 2 for the Selective Inhibitors ALX1393 and ORG25543. ACS Chem Neurosci *12*, 1860-1872. 10.1021/acschemneuro.0c00602.
17. Caulfield, W.L., Collie, I.T., Dickins, R.S., Epemolu, O., McGuire, R., Hill, D.R., McVey, G., Morphy, J.R., Rankovic, Z., and Sundaram, H. (2001). The First Potent and Selective Inhibitors of the Glycine Transporter Type 2. Journal of Medicinal Chemistry *44*, 2679-2682. 10.1021/jm0011272.
18. Cantwell Chater, R., Quinn, A.S., Wilson, K., Frangos, Z.J., Sutton, P., Jayakumar, S., Cioffi, C.L., O'Mara, M.L., and Vandenberg, R.J. (2023). The efficacy of the analgesic GlyT2 inhibitor, ORG25543, is determined by two connected allosteric sites. J Neurochem. 10.1111/jnc.16028.
19. Jeong, H.J., Vandenberg, R.J., and Vaughan, C.W. (2010). N-arachidonyl-glycine modulates synaptic transmission in superficial dorsal horn. Br J Pharmacol *161*, 925-935. 10.1111/j.1476-5381.2010.00935.x.
20. Lee, H.J., Sim, J.Y., Song, I., Nedeljkovic, S.S., Kim, D.K., Oh, A.Y., Yoon, S.Z., Moon, Y.J., Park, M., Park, I., et al. (2024). Reduction of postoperative pain and opioid consumption by VVZ-149, first-in-class analgesic molecule: A confirmatory phase 3 trial of laparoscopic colectomy. J Clin Anesth *101*, 111729. 10.1016/j.jclinane.2024.111729.
21. Nedeljkovic, S.S., Song, I., Bao, X., Zeballos, J.L., Correll, D.J., Zhang, Y., Ledley, J.S., Bhandari, A., Bai, X., Lee, S.R., and Cho, S. (2022). Exploratory study of VVZ-149, a novel analgesic molecule, in the affective component of acute postoperative pain after laparoscopic colorectal surgery. J Clin Anesth *76*, 110576. 10.1016/j.jclinane.2021.110576.
22. Arribas-Gonzalez, E., de Juan-Sanz, J., Aragon, C., and Lopez-Corcuera, B. (2015). Molecular basis of the dominant negative effect of a glycine transporter 2 mutation associated with hyperekplexia. J Biol Chem *290*, 2150-2165. 10.1074/jbc.M114.587055.
23. Morrow, J.A., Collie, I.T., Dunbar, D.R., Walker, G.B., Shahid, M., and Hill, D.R. (1998). Molecular cloning and functional expression of the human glycine transporter GlyT2 and chromosomal localisation of the gene in the human genome. FEBS Lett *439*, 334-340. 10.1016/s0014-5793(98)01390-8.
24. Jardetzky, O. (1966). Simple allosteric model for membrane pumps. Nature *211*, 969-970. 10.1038/211969a0.
25. Subramanian, N., Scopelitti, A.J., Carland, J.E., Ryan, R.M., O'Mara, M.L., and Vandenberg, R.J. (2016). Identification of a 3rd Na+ Binding Site of the Glycine Transporter, GlyT2. PLoS One *11*, e0157583. 10.1371/journal.pone.0157583.
26. Erdem, F.A., Ilic, M., Koppensteiner, P., Golacki, J., Lubec, G., Freissmuth, M., and Sandtner, W. (2019). A comparison of the transport kinetics of glycine transporter 1 and glycine transporter 2. J Gen Physiol *151*, 1035-1050. 10.1085/jgp.201912318.
27. Benito-Munoz, C., Perona, A., Abia, D., Dos Santos, H.G., Nunez, E., Aragon, C., and Lopez-Corcuera, B. (2018). Modification of a Putative Third Sodium Site in the Glycine Transporter GlyT2 Influences the Chloride Dependence of Substrate Transport. Front Mol Neurosci *11*, 347. 10.3389/fnmol.2018.00347.
28. Shahsavar, A., Stohler, P., Bourenkov, G., Zimmermann, I., Siegrist, M., Guba, W., Pinard, E., Sinning, S., Seeger, M.A., Schneider, T.R., et al. (2021). Structural insights into the inhibition of glycine reuptake. Nature *591*, 677-681. 10.1038/s41586-021-03274-z.
29. Motiwala, Z., Aduri, N.G., Shaye, H., Han, G.W., Lam, J.H., Katritch, V., Cherezov, V., and Gati, C. (2022). Structural basis of GABA reuptake inhibition. Nature *606*, 820-826. 10.1038/s41586-022-04814-x.

30. Li, Y., Wang, X., Meng, Y., Hu, T., Zhao, J., Li, R., Bai, Q., Yuan, P., Han, J., Hao, K., et al. (2024). Dopamine reuptake and inhibitory mechanisms in human dopamine transporter. Nature *632*, 686-694. 10.1038/s41586-024-07796-0.
31. Singh, I., Seth, A., Billesbolle, C.B., Braz, J., Rodriguiz, R.M., Roy, K., Bekele, B., Craik, V., Huang, X.P., Boytsov, D., et al. (2023). Structure-based discovery of conformationally selective inhibitors of the serotonin transporter. Cell *186*, 2160-2175 e2117. 10.1016/j.cell.2023.04.010.
32. Nielsen, J.C., Salomon, K., Kalenderoglou, I.E., Bargmeyer, S., Pape, T., Shahsavar, A., and Loland, C.J. (2024). Structure of the human dopamine transporter in complex with cocaine. Nature *632*, 678-685. 10.1038/s41586-024-07804-3.
33. Coleman, J.A., Green, E.M., and Gouaux, E. (2016). X-ray structures and mechanism of the human serotonin transporter. Nature *532*, 334-339. 10.1038/nature17629.
34. Penmatsa, A., Wang, K.H., and Gouaux, E. (2013). X-ray structure of dopamine transporter elucidates antidepressant mechanism. Nature *503*, 85-90. 10.1038/nature12533.
35. Srivastava, D.K., Navratna, V., Tosh, D.K., Chinn, A., Sk, M.F., Tajkhorshid, E., Jacobson, K.A., and Gouaux, E. (2024). Structure of the human dopamine transporter and mechanisms of inhibition. Nature *632*, 672-677. 10.1038/s41586-024-07739-9.
36. Wang, K.H., Penmatsa, A., and Gouaux, E. (2015). Neurotransmitter and psychostimulant recognition by the dopamine transporter. Nature *521*, 322-327. 10.1038/nature14431.
37. Plenge, P., Yang, D., Salomon, K., Laursen, L., Kalenderoglou, I.E., Newman, A.H., Gouaux, E., Coleman, J.A., and Loland, C.J. (2021). The antidepressant drug vilazodone is an allosteric inhibitor of the serotonin transporter. Nat Commun *12*, 5063. 10.1038/s41467-021-25363-3.
38. Pedersen, C.N., Yang, F., Ita, S., Xu, Y., Akunuri, R., Trampari, S., Neumann, C.M.T., Desdorf, L.M., Schiott, B., Salvino, J.M., et al. (2024). Cryo-EM structure of the dopamine transporter with a novel atypical non-competitive inhibitor bound to the orthosteric site. J Neurochem *168*, 2043-2055. 10.1111/jnc.16179.
39. Hu, T., Yu, Z., Zhao, J., Meng, Y., Salomon, K., Bai, Q., Wei, Y., Zhang, J., Xu, S., Dai, Q., et al. (2024). Transport and inhibition mechanisms of the human noradrenaline transporter. Nature *632*, 930-937. 10.1038/s41586-024-07638-z.
40. Wei, Y., Li, R., Meng, Y., Hu, T., Zhao, J., Gao, Y., Bai, Q., Li, N., and Zhao, Y. (2024). Transport mechanism and pharmacology of the human GlyT1. Cell *187*, 1719-1732 e1714. 10.1016/j.cell.2024.02.026.
41. Vandenberg, R.J., Shaddick, K., and Ju, P. (2007). Molecular basis for substrate discrimination by glycine transporters. J Biol Chem *282*, 14447-14453. 10.1074/jbc.M609158200.
42. Tonge, P.J. (2018). Drug-Target Kinetics in Drug Discovery. ACS Chem Neurosci *9*, 29-39. 10.1021/acschemneuro.7b00185.
43. Cusack, K.P., Wang, Y., Hoemann, M.Z., Marjanovic, J., Heym, R.G., and Vasudevan, A. (2015). Design strategies to address kinetics of drug binding and residence time. Bioorg Med Chem Lett *25*, 2019-2027. 10.1016/j.bmcl.2015.02.027.
44. Girotto, G.L., Vicente, C.T., Miryam, P., Susana, B., Alberto, P.J., Armando, V.R., Max, S., and Manuel, M. (2020). The N-terminal tail of the glycine transporter: role in transporter phosphorylation. Med Res Arch *8*. 10.18103/mra.v8i5.2085.
45. Yamashita, A., Singh, S.K., Kawate, T., Jin, Y., and Gouaux, E. (2005). Crystal structure of a bacterial homologue of Na+/Cl--dependent neurotransmitter transporters. Nature *437*, 215-223. 10.1038/nature03978.
46. Genheden, S., and Ryde, U. (2015). The MM/PBSA and MM/GBSA methods to estimate ligand-binding affinities. Expert Opin Drug Discov *10*, 449-461. 10.1517/17460441.2015.1032936.
47. Srinivasan, J., Cheatham, T.E., Cieplak, P., Kollman, P.A., and Case, D.A. (1998). Continuum solvent studies of the stability of DNA, RNA, and phosphoramidate− DNA helices. Journal of the American Chemical Society *120*, 9401-9409.

48. Massova, I., and Kollman, P.A. (2000). Combined molecular mechanical and continuum solvent approach (MM-PBSA/GBSA) to predict ligand binding. Perspectives in drug discovery and design *18*, 113-135.
49. Hao, M.H., Haq, O., and Muegge, I. (2007). Torsion angle preference and energetics of small-molecule ligands bound to proteins. J Chem Inf Model *47*, 2242-2252. 10.1021/ci700189s.
50. Malinauskaite, L., Quick, M., Reinhard, L., Lyons, J.A., Yano, H., Javitch, J.A., and Nissen, P. (2014). A mechanism for intracellular release of Na+ by neurotransmitter/sodium symporters. Nat Struct Mol Biol *21*, 1006-1012. 10.1038/nsmb.2894.
51. Coleman, J.A., Yang, D., Zhao, Z., Wen, P.C., Yoshioka, C., Tajkhorshid, E., and Gouaux, E. (2019). Serotonin transporter-ibogaine complexes illuminate mechanisms of inhibition and transport. Nature *569*, 141-145. 10.1038/s41586-019-1135-1.
52. Tan, J., Xiao, Y., Kong, F., Zhang, X., Xu, H., Zhu, A., Liu, Y., Lei, J., Tian, B., Yuan, Y., and Yan, C. (2024). Molecular basis of human noradrenaline transporter reuptake and inhibition. Nature *632*, 921-929. 10.1038/s41586-024-07719-z.
53. Frangos, Z.J., Wilson, K.A., Aitken, H.M., Cantwell Chater, R., Vandenberg, R.J., and O'Mara, M.L. (2023). Membrane cholesterol regulates inhibition and substrate transport by the glycine transporter, GlyT2. Life Sci Alliance *6*. 10.26508/lsa.202201708.
54. Hong, W.C., and Amara, S.G. (2010). Membrane cholesterol modulates the outward facing conformation of the dopamine transporter and alters cocaine binding. J Biol Chem *285*, 32616-32626. 10.1074/jbc.M110.150565.
55. Jones, K.T., Zhen, J., and Reith, M.E. (2012). Importance of cholesterol in dopamine transporter function. J Neurochem *123*, 700-715. 10.1111/jnc.12007.
56. Bjerregaard, H., Severinsen, K., Said, S., Wiborg, O., and Sinning, S. (2015). A dualistic conformational response to substrate binding in the human serotonin transporter reveals a high affinity state for serotonin. J Biol Chem *290*, 7747-7755. 10.1074/jbc.M114.573477.
57. Scanlon, S.M., Williams, D.C., and Schloss, P. (2001). Membrane cholesterol modulates serotonin transporter activity. Biochemistry *40*, 10507-10513. 10.1021/bi010730z.
58. Magnani, F., Tate, C.G., Wynne, S., Williams, C., and Haase, J. (2004). Partitioning of the serotonin transporter into lipid microdomains modulates transport of serotonin. J Biol Chem *279*, 38770-38778. 10.1074/jbc.M400831200.
59. Nunez, E., Alonso-Torres, P., Fornes, A., Aragon, C., and Lopez-Corcuera, B. (2008). The neuronal glycine transporter GLYT2 associates with membrane rafts: functional modulation by lipid environment. J Neurochem *105*, 2080-2090. 10.1111/j.1471-4159.2008.05292.x.
60. Liu, X., Mitrovic, A.D., and Vandenberg, R.J. (2009). Glycine transporter 1 associates with cholesterol-rich membrane raft microdomains. Biochem Biophys Res Commun *384*, 530-534. 10.1016/j.bbrc.2009.05.014.
61. Zeppelin, T., Ladefoged, L.K., Sinning, S., Periole, X., and Schiott, B. (2018). A direct interaction of cholesterol with the dopamine transporter prevents its out-to-inward transition. PLoS Comput Biol *14*, e1005907. 10.1371/journal.pcbi.1005907.
62. Pang, M.H., Kim, Y., Jung, K.W., Cho, S., and Lee, D.H. (2012). A series of case studies: practical methodology for identifying antinociceptive multi-target drugs. Drug Discov Today *17*, 425-434. 10.1016/j.drudis.2012.01.003.
63. Mostyn, S.N., Wilson, K.A., Schumann-Gillett, A., Frangos, Z.J., Shimmon, S., Rawling, T., Ryan, R.M., O'Mara, M.L., and Vandenberg, R.J. (2019). Identification of an allosteric binding site on the human glycine transporter, GlyT2, for bioactive lipid analgesics. Elife *8*. 10.7554/eLife.47150.
64. Wiles, A.L., Pearlman, R.J., Rosvall, M., Aubrey, K.R., and Vandenberg, R.J. (2006). N-Arachidonyl-glycine inhibits the glycine transporter, GLYT2a. J Neurochem *99*, 781-786. 10.1111/j.1471-4159.2006.04107.x.

65. Punjani, A., Rubinstein, J.L., Fleet, D.J., and Brubaker, M.A. (2017). cryoSPARC: algorithms for rapid unsupervised cryo-EM structure determination. Nat Methods *14*, 290-296. 10.1038/nmeth.4169.
66. Emsley, P., Lohkamp, B., Scott, W.G., and Cowtan, K. (2010). Features and development of Coot. Acta Crystallogr D Biol Crystallogr *66*, 486-501. 10.1107/S0907444910007493.
67. Liebschner, D., Afonine, P.V., Baker, M.L., Bunkoczi, G., Chen, V.B., Croll, T.I., Hintze, B., Hung, L.W., Jain, S., McCoy, A.J., et al. (2019). Macromolecular structure determination using X-rays, neutrons and electrons: recent developments in Phenix. Acta Crystallogr D Struct Biol *75*, 861-877. 10.1107/S2059798319011471.
68. Pettersen, E.F., Goddard, T.D., Huang, C.C., Meng, E.C., Couch, G.S., Croll, T.I., Morris, J.H., and Ferrin, T.E. (2021). UCSF ChimeraX: Structure visualization for researchers, educators, and developers. Protein Sci *30*, 70-82. 10.1002/pro.3943.
69. Croll, T.I. (2018). ISOLDE: a physically realistic environment for model building into low-resolution electron-density maps. Acta Crystallogr D Struct Biol *74*, 519-530. 10.1107/S2059798318002425.
70. Kidmose, R.T., Juhl, J., Nissen, P., Boesen, T., Karlsen, J.L., and Pedersen, B.P. (2019). Namdinator - automatic molecular dynamics flexible fitting of structural models into cryo-EM and crystallography experimental maps. IUCrJ *6*, 526-531. 10.1107/S2052252519007619.
71. Schmid, N., Eichenberger, A.P., Choutko, A., Riniker, S., Winger, M., Mark, A.E., and van Gunsteren, W.F. (2011). Definition and testing of the GROMOS force-field versions 54A7 and 54B7. Eur Biophys J *40*, 843-856. 10.1007/s00249-011-0700-9.
72. Tribello, G.A., Bonomi, M., Branduardi, D., Camilloni, C., and Bussi, G. (2014). PLUMED 2: New feathers for an old bird. Computer Physics Communications *185*, 604-613. https://doi.org/10.1016/j.cpc.2013.09.018.
73. PLUMED Consortium (2019). Promoting transparency and reproducibility in enhanced molecular simulations. Nat Methods *16*, 670-673. 10.1038/s41592-019-0506-8.
74. Humphrey, W., Dalke, A., and Schulten, K. (1996). VMD: visual molecular dynamics. J Mol Graph *14*, 33-38, 27-38. 10.1016/0263-7855(96)00018-5.
75. Sondergaard, C.R., Olsson, M.H., Rostkowski, M., and Jensen, J.H. (2011). Improved Treatment of Ligands and Coupling Effects in Empirical Calculation and Rationalization of pKa Values. J Chem Theory Comput *7*, 2284-2295. 10.1021/ct200133y.
76. Olsson, M.H., Sondergaard, C.R., Rostkowski, M., and Jensen, J.H. (2011). PROPKA3: Consistent Treatment of Internal and Surface Residues in Empirical pKa Predictions. J Chem Theory Comput *7*, 525-537. 10.1021/ct100578z.
77. Stroet, M., Caron, B., Visscher, K.M., Geerke, D.P., Malde, A.K., and Mark, A.E. (2018). Automated Topology Builder Version 3.0: Prediction of Solvation Free Enthalpies in Water and Hexane. J Chem Theory Comput *14*, 5834-5845. 10.1021/acs.jctc.8b00768.
78. Pan, X., Wang, H., Li, C., Zhang, J.Z.H., and Ji, C. (2021). MolGpka: A Web Server for Small Molecule pK(a) Prediction Using a Graph-Convolutional Neural Network. J Chem Inf Model *61*, 3159-3165. 10.1021/acs.jcim.1c00075.
79. Knight, C.J., and Hub, J.S. (2015). MemGen: a general web server for the setup of lipid membrane simulation systems. Bioinformatics *31*, 2897-2899. 10.1093/bioinformatics/btv292.
80. Kumari, R., Kumar, R., Open Source Drug Discovery, C., and Lynn, A. (2014). g_mmpbsa--a GROMACS tool for high-throughput MM-PBSA calculations. J Chem Inf Model *54*, 1951-1962. 10.1021/ci500020m.
81. Baker, N.A., Sept, D., Joseph, S., Holst, M.J., and McCammon, J.A. (2001). Electrostatics of nanosystems: application to microtubules and the ribosome. Proc Natl Acad Sci U S A *98*, 10037-10041. 10.1073/pnas.181342398.
82. Gowers, R.J., Linke, M., Barnoud, J., Reddy, T.J.E., Melo, M.N., Seyler, S.L., Domanski, J., Dotson, D.L., Buchoux, S., Kenney, I.M., and Beckstein, O. (2019). MDAnalysis: A Python Package for the Rapid Analysis of Molecular Dynamics

Simulations. Conference: PROC. OF THE 15th PYTHON IN SCIENCE CONF. (SCIPY 2016) ; 2016-07-11 - 2016-07-11 ;. Los Alamos National Laboratory (LANL), Los Alamos, NM (United States).
83. Punjani, A., Zhang, H., and Fleet, D.J. (2020). Non-uniform refinement: adaptive regularization improves single-particle cryo-EM reconstruction. Nat Methods *17*, 1214-1221. 10.1038/s41592-020-00990-8.
84. Jumper, J., Evans, R., Pritzel, A., Green, T., Figurnov, M., Ronneberger, O., Tunyasuvunakool, K., Bates, R., Zidek, A., Potapenko, A., et al. (2021). Highly accurate protein structure prediction with AlphaFold. Nature *596*, 583-589. 10.1038/s41586-021-03819-2.
85. Bennett, G.J., and Xie, Y.K. (1988). A peripheral mononeuropathy in rat that produces disorders of pain sensation like those seen in man. Pain *33*, 87-107. 10.1016/0304-3959(88)90209-6.
86. Seltzer, Z., Dubner, R., and Shir, Y. (1990). A novel behavioral model of neuropathic pain disorders produced in rats by partial sciatic nerve injury. Pain *43*, 205-218. 10.1016/0304-3959(90)91074-S.
87. McKendrick, G., Garrett, H., Jones, H.E., McDevitt, D.S., Sharma, S., Silberman, Y., and Graziane, N.M. (2020). Ketamine Blocks Morphine-Induced Conditioned Place Preference and Anxiety-Like Behaviors in Mice. Front Behav Neurosci *14*, 75. 10.3389/fnbeh.2020.00075.
88. Automated Topology Builder (ATB) and Repository-C31H49O4 | MD Topology | NMR | X-Ray. https://atb.uq.edu.au/molecule.py?molid=1736730.
89. Automated Topology Builder (ATB) and Repository-C24H33N2O4 | MD Topology | NMR | X-Ray.
90. Automated Topology Builder (ATB) and Repository-molid 1732579|MD Topology | NMR | X-Ray. https://atb.uq.edu.au/molecule.py?molid=1732579.
91. Hermans, J., Berendsen, H.J.C., Van Gunsteren, W.F., and Postma, J.P.M. (1984). A consistent empirical potential for water–protein interactions. Biopolymers *23*, 1513-1518. https://doi.org/10.1002/bip.360230807.
92. Feenstra, K.A., Hess, B., and Berendsen, H.J.C. (1999). Improving efficiency of large time-scale molecular dynamics simulations of hydrogen-rich systems. J Comput Chem *20*, 786-798. 10.1002/(SICI)1096-987X(199906)20:8<786::AID-JCC5>3.0.CO;2-B.
93. Bussi, G., Donadio, D., and Parrinello, M. (2007). Canonical sampling through velocity rescaling. J Chem Phys *126*, 014101. 10.1063/1.2408420.
94. Parrinello, M., and Rahman, A. (1980). Crystal Structure and Pair Potentials: A Molecular-Dynamics Study. Physical Review Letters *45*, 1196-1199. 10.1103/PhysRevLett.45.1196.
95. Miyamoto, S., and Kollman, P.A. (1992). Settle: An analytical version of the SHAKE and RATTLE algorithm for rigid water models. Journal of Computational Chemistry *13*, 952-962. https://doi.org/10.1002/jcc.540130805.
96. Hess, B. (2008). P-LINCS: A Parallel Linear Constraint Solver for Molecular Simulation. J Chem Theory Comput *4*, 116-122. 10.1021/ct700200b.
97. Wang, E., Sun, H., Wang, J., Wang, Z., Liu, H., Zhang, J.Z., and Hou, T. (2019). End-point binding free energy calculation with MM/PBSA and MM/GBSA: strategies and applications in drug design. Chemical reviews *119*, 9478-9508.
98. Kumari, R., Kumar, R., Consortium, O.S.D.D., and Lynn, A. (2014). g_mmpbsa□ A GROMACS tool for high-throughput MM-PBSA calculations. Journal of chemical information and modeling *54*, 1951-1962.
99. Jurrus, E., Engel, D., Star, K., Monson, K., Brandi, J., Felberg, L.E., Brookes, D.H., Wilson, L., Chen, J., Liles, K., et al. (2018). Improvements to the APBS biomolecular solvation software suite. Protein Sci *27*, 112-128. 10.1002/pro.3280.
100. Krauth, W. (2006). Statistical mechanics: algorithms and computations (OUP Oxford).
101. Sharp, K.A., and Honi, B. (1990). Interactions in macromolecules: theory and applications. Annu. Rev. Biophys. Biophys. Chem *19*, 32.